Effects of Variations in Boundary Current Strength on Export Pathways of Convected Water Masses in the Labrador Sea

by

P.H. (Nick) van de Voort

Research Project

06-07-2021

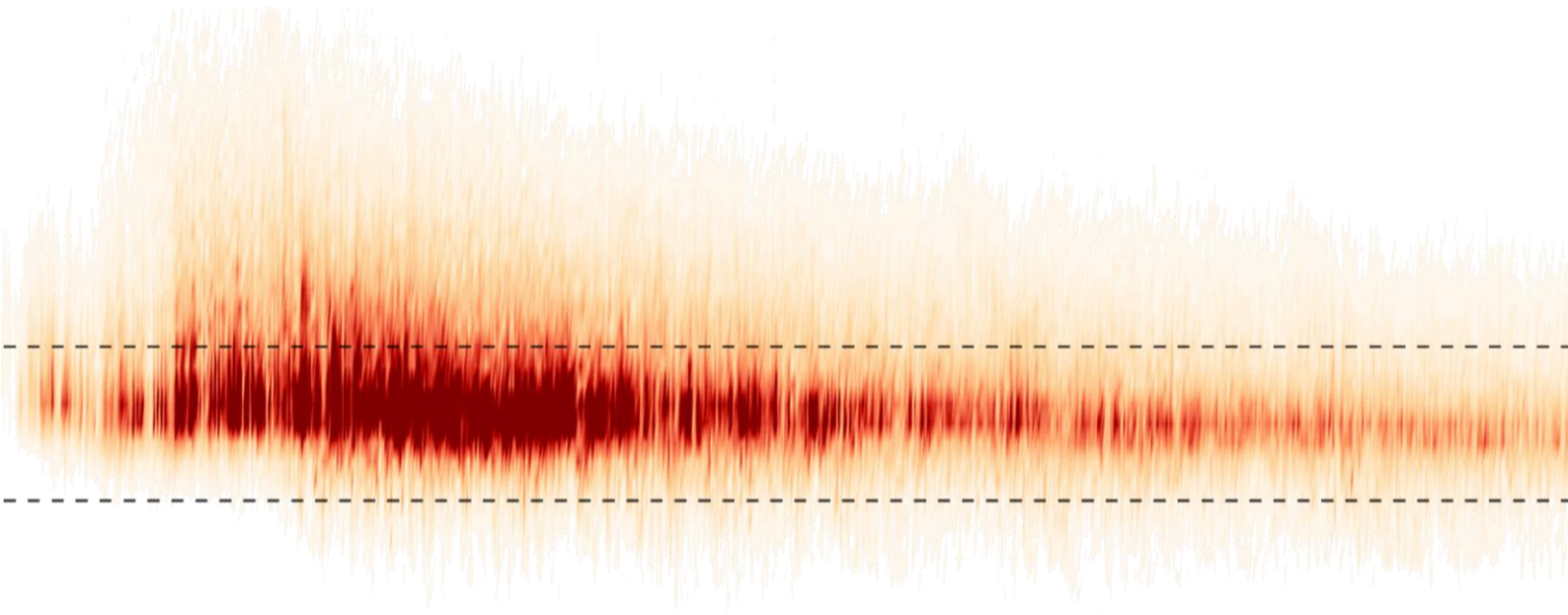

Supervisors:

Dr. C.A. Katsman	Environmental Fluid Mechanics Delft University of Technology
Dr. S. Georgiou	Geoscience and Remote Sensing Delft University of Technology

TU Delft

ABSTRACT

The production of water masses formed by convection in the Labrador Sea (i.e. Labrador Sea Water, LSW) and its variability contributes to the variability of the Atlantic Meridional Overturning Circulation (AMOC). Several studies put the role of the Labrador Sea under renewed debate, and suggest a rather complex interplay between the production of the LSW, the boundary current and the eddy field. To this end, an increased effort is put in understanding the variability of the LSW, its export routes and associated export timescales. In this study, the effects of variations in boundary current strength on the export pathways of convected water masses are investigated. The same idealized eddy-resolving numerical model is used as Georgiou et al. (2019) which has proven to be capable of capturing the key dynamics of the Labrador Sea, like the annual cycle of convection, the process and timescales of restratification, and properties of the mesoscale eddy field. Model simulations are set-up with different scenarios of the density structure of the boundary current at inflow location (i.e. southern tip of Greenland). The variations result in respectively a 5% strengthening and 5% weakening of the boundary current, which corresponds to interannual variability of observed surface velocities. The model output demonstrates that boundary current variations start a chain of reactions, significantly changing the dynamics of the Labrador Sea. This has implications for deep convection processes in the interior of the basin and thus the export product. With a passive tracer analysis it is shown that convected water masses formed in the convection area are laterally steered along isopycnals by an eddy-induced shear flow from the interior towards the boundary current at the West-Greenland coast in deeper layers. A strengthening (weakening) of the boundary current yields a lighter (denser) water mass to be exported at shallower (deeper) layers out of the interior. The most intense entrainment into the boundary current occurs where both the density and depth of the convected water masses match the local water mass properties of the boundary current, and where eddies detach from the boundary current. The associated export timescales can be linked to the location where eddies detach, and to the strength of the eddy-induced shear flow. This study further highlights the implications for linking variability in the LSW production and export to AMOC variability as the total export of convected waters in the Labrador Sea is a mixture of multiyear convected waters. Based on density alone, measurements of water masses at the exit do not directly reveal the past-year dynamical state of the Labrador Sea. This emphasizes that a proper representation of mesoscale eddies in models is necessary for representing the export timescales and water mass properties of the LSW, and their response to changing forcing.

CONTENTS

CHAPTER 1

INTRODUCTION

This chapter gives an overview of the state-of-the-art research regarding the Labrador Sea dynamics and its role for the Atlantic Meridional Overturning Circulation. The proposed research question and approach of this study aim to bridge the knowledge gap in the understanding of the effect of boundary current variations on export pathways of convective waters.

1.1. Scientific background

In the North Atlantic Ocean, lighter waters originating from the subtropics transform to denser waters, and flow southwards in deeper layers in a circulation pattern known as the Atlantic Meridional Overturning Circulation (AMOC, Figure 1.1). This circulation quantifies the zonally integrated meridional volume transport of water masses in the Atlantic Ocean. Its strength is commonly estimated as the total northward transport in the upper $1000\,m$ of the water column (Georgiou, et al., 2020), roughly to be 18 Sverdrup (Sv, $1\ \mathrm{Sv} = 10^6\,m^3/s$) (Cunningham, et al., 2007; Georgiou, et al., 2019). The strength of this thermohaline circulation is set by temperature (thermo) and salinity (haline) variations, but the only place where temperature and salinity change is at the surface. On their journey northwards the surface waters release heat to the atmosphere (upper AMOC limb, red path in Figure 1.1). When surface waters cool they become denser. Once they get denser than the waters beneath them, a statically unstable situation occurs (i.e. unstable stratification). Vertical mixing with deeper waters makes the situation stable again. The process is called 'deep convection'. Eventually, the newly formed cold water masses return southwards at depth and feed the lower AMOC limb (blue path in Figure 1.1). The process of deep convection is a key factor in setting the strength of the overturning circulation.

Figure 1.1 Schematization of the Atlantic Meridional Overturning Circulation (AMOC). In the upper layers, relatively warm waters flow northwards (red). In deeper layers, cold waters return southwards (blue). Deep convection zones are highlighted with the blue dots (Irminger Sea and Labrador Sea). From: The National Oceanography Centre (2018).

The lower limb of the AMOC contains water masses that can be traced back to locations where deep ocean convection occurs. The most important ones are the marginal seas of the North Atlantic. Those are regions where surface waters become denser during wintertime, and consequently mix vertically

with deeper layers (Marshall & Schott, 1999). There are only a few locations in the ocean where dense waters are formed, including the Labrador Sea and the Irminger Sea.

The product of water mass transformation in the Labrador Sea is labeled as Labrador Sea Water (LSW). The Labrador Sea is located between West-Greenland and the Canadian peninsula Labrador. It is characterized by a relatively strong cyclonic boundary current encircling the marginal sea basin. This current is a confluence of the warm, salty Irminger Current (IC) and the cold, fresh East Greenland Current (EGG, Figure 1.2). The currents continue their route as the West Greenland Current (WGC), but keep the differences in thermohaline properties. The product of the lower limb of the AMOC is a combination of the Labrador Sea Water (LSW) and overflow waters (i.e. Denmark Strait Overflow Water (DSOW) and Iceland Scotland Overflow Water (ISOW)) from the subpolar North Atlantic. The production of the LSW and its variability is considered to be a potential driver for AMOC variability in overturning (Georgiou, et al., 2020), and because recent state-of-the-art climate models project a substantial weakening of the AMOC over the 21st century, an increased effort is put in understanding this driver (Georgiou, et al., 2021).

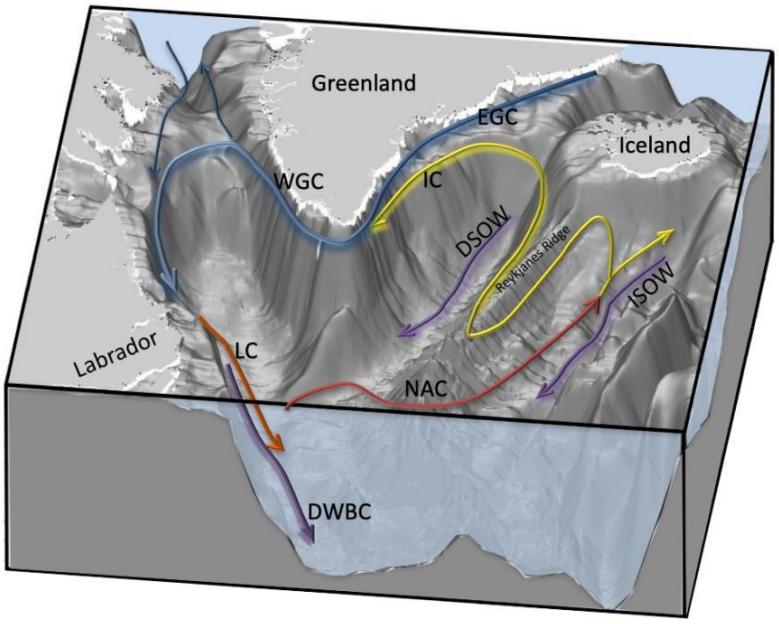

Figure 1.2 Sea-floor topography of the subpolar North Atlantic (SPNA) compiled from ETOPO1 data (Amante and Eakins, 2009) and schematized current system: EGC and WGC: East and West Greenland Currents, respectively. IC: Irminger Current, LC: Labrador Current, NAC: North Atlantic Current, DSOW: Denmark Strait Overflow Water, ISOW: Iceland Scotland Overflow Water and DWBC: Deep Western Boundary Current. From (Georgiou, 2021).

The climatic role of the AMOC stems from the northward transport of warm and salty surface waters, bringing a significant amount of heat to higher latitudes, thereby setting the mild climate conditions in Western Europe (via prevailing westerly winds). Moreover, the overturning is a key process in controlling the interaction and distribution of biogeochemical tracers (e.g. carbon dioxide) that determine atmospheric temperatures (Gruber, et al., 2019).

Traditionally, a close connection between the water mass transformation in the Labrador Sea and AMOC variability was suggested in earlier modeling studies (Biastoch, et al., 2008; Zhang, 2010). However,

more up-to-date observations and numerical studies put the potential connection under renewed debate (Georgiou, et al., 2020), suggesting a rather complex relation between the two. This is partly due to the limited understanding on how the LSW leaves the Labrador Sea. In particular, the existence of multiple export routes and the associated timescales creates a complex linkage to AMOC variability.

At first glance, sinking of dense water masses occurs in the interior of the Labrador Sea. But applying the thermodynamic and vorticity balances in idealized models shows that at high latitudes extremely strong horizontal geostrophic currents would be needed in order to balance widespread downwelling in the interior (Spall & Pickart, 2001). According to Spall and Pickart (2001), downwelling is possible along steep topographic slopes where vortex stretching of the nearly horizontal non-divergent flow is balanced by friction (i.e. ageostrophic flow).

Recent highly idealized numerical studies of a convective marginal sea (e.g., Brüggemann & Katsman, 2019; Georgiou, et al., 2019) and realistic model studies (e.g., Katsman, et al., 2018) have shown that downwelling indeed occurs along the perimeter of the marginal sea. They found an enhanced signal of downwelling in regions characterized by strong eddy activity, in particular at the West-Greenland coast. Eddies that are triggered by steepening of the topography along the West-Greenland coast are referred to as Irminger Rings (IRs). IRs are known to be very energetic, long-living, and transport the warmer, saline Irminger Current (IC) to the area of deep convection, and are therefore essential for restratification of the interior after wintertime convection (Gelderloos, et al., 2011). At the same time, IRs are known to play a crucial role in re-entrainment of denser convective waters into the boundary current (Georgiou, 2021). Brüggemann and Katsman (2019) confirm that the densest water masses are laterally steered (along isopycnals i.e. lines of constant density) from their formation location (interior) towards this region of high eddy activity. In this region the isopycnals are strongly tilted due to the topographic narrowing, inducing the along-isopycnal flow to transport convective water masses to deeper layers where they are being entrained in the boundary current. This entrainment can only take place where the density and depth of dense water masses match the local water mass properties of the boundary current (Georgiou, et al., 2021). At the same time, the boundary current sheds eddies that advect buoyant water from the boundary current to the interior of the basin, contributing to the restratification of the water column after convection. The presence of eddies near the coast of West-Greenland effectively block the re-entrainment of lighter convective waters in the boundary current. These lighter convective waters are located at shallower depth. The denser convective waters can potentially re-entrain the boundary current at the West-Greenland coast. This results in different pathways that water masses follow prior to exiting the Labrador Sea. Most importantly, Brüggemann and Katsman (2019), Georgiou et al., (2020, 2021), highlight an indirect route that the densest water masses take (which is associated with longer residence and export timescales) that involves boundary-interior interaction (path 3 in Figure 1.3). In contrast, the lighter water masses formed close to or in the boundary current are exported faster, following a more direct route (path 1 and 2 in Figure 1.3). According to Brüggemann and Katsman (2019), the associated overturning mechanism differs for these paths. Path 1 involves diapycnal mixing in the boundary current itself, which are relatively light water masses with high export rates. Path 2 and 3 involve boundary current-interior interaction with more complex interplays and residence times.

The above highlights that care should be taken when linking AMOC variability to variability in LSW production. The differences in timescales of convective waters to exit the Labrador Sea depends on the pathway and location where these water masses can re-enter the boundary current. It is a complex three-dimensional picture in which the interior-boundary interaction is crucial for the overturning of the densest LSW that contributes to the lower limb of the AMOC. To this end, the oceanographic community aims gain a better understanding of the processes that control the transports along these

various pathways and the variability therein, therewith linking variability in the Labrador Sea and variability in the North Atlantic overturning.

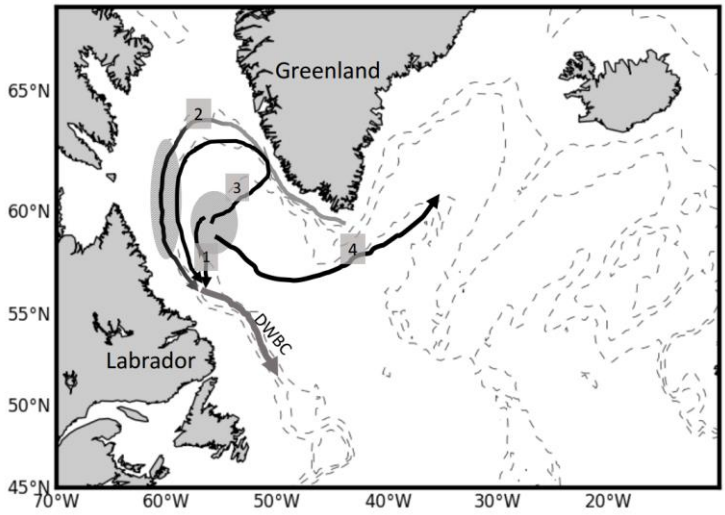

Figure 1.3 Schematic of the pathways of the LSW: (1) direct entrainment of the LSW in the boundary current, (2) LSW formation within the boundary current, (3) eddy-driven LSW transport from the interior towards the West-Greenland shelf, and (4) mid-depth recirculation of the LSW towards the Irminger Sea. The shaded grey areas indicate locations of convection in the Labrador Sea. The dashed grey lines are isobath contour lines (with contour interval $1000m$ starting from the isobath of $1000\ m$. From (Georgiou, 2021).

According to Brüggemann and Katsman (2019) the efficiency of each export route depends on multiple factors:

- Strength of the surface heat loss;
- Stratification and strength of the boundary current;
- Location of the deep convection areas;
- Location and strength of the eddy activity (where downwelling occurs).

Recent progress is made assessing the relative importance of the above factors for the export of LSW by making use of idealized models. Georgiou et al. (2021) investigated the sensitivity of water mass transformation process due to changes in surface forcing. They revealed an apparent signal in the net overturning strength due to changes in both the depth of convection and the eddy field in the Labrador Sea. This led to different export routes. Latest research by Georgiou (2021), using an idealized numerical set-up showed that both the transport volume and the transformation rates are altered by changes in surface forcing. Meanwhile, the along-isopycnal, lateral transport is still constrained by a match between density and depth of the LSW in the interior and the density structure of the boundary current. Consequently, the relative importance of the direct and indirect routes is affected non-linearly with respect to changes in surface forcing (Georgiou, 2021). In view of the affected export pathways and associated timescales, the non-linear response adds to the complexity in understanding the AMOC variability.

Another interesting notion is to analyze how changes in the inflow boundary conditions affect the water mass transformation process and export pathways in the Labrador Sea. As entrainment of convective water in the boundary current is constrained by matching density and depth of the LSW in the interior and the density structure of the boundary current, changes in this structure hypothetically open and/or

close potential export pathways. The idealized model of Georgiou et al. (2019) provides the opportunity to analyze variations in the boundary current structure.

In this study, numerical modelling strongly builds on the idealized model of Georgiou et al. (2019) in order to provide new insight on the relationship between boundary current inflow conditions and water mass transformation, and the export and associated timescales of deep water masses. To that end, the study addresses with the following question:

What is the effect of variations in boundary current strength on export pathways of convective water masses in the Labrador?

1.2. Hypothesis

In order to investigate how variations in the boundary current potentially lead to different export pathways one needs to gain understanding on the physics that govern the boundary current system. Following earlier studies of Georgiou (2021), an idealized eddy-resolving model is used that aids our understanding of the Labrador Sea dynamics (more about the approach in Section 1.4).

The strength of the boundary current is set by the horizontal density gradient between the buoyant boundary current and the denser interior. At this scale, the thermal wind balance holds (in geostrophic balance) and induces a shear velocity profile in the vertical, which is perpendicular to the horizontal density gradients associated with it. Chapter 2 will elaborate more on the balancing forces, the density structure and zonal velocities of the inflowing boundary current in the Labrador Sea.

During its journey along the perimeter of the basin, the boundary current cools due to surface heat loss and lateral eddy heat fluxes (i.e. the boundary current sheds eddies along the density interface with the interior, with high intensity along the topographic narrowing due to barotropic instabilities). The change in horizontal density gradients associated with the cooling, cause the boundary current to slow down in the surface layer, and accelerate in deeper layers (i.e. the current becomes more barotropic). According to Brüggemann and Katsman (2019), the stratification and strength of the boundary current impacts the location and strength of the eddy activity. This has implications for the role eddies play in lateral heat exchange and export of convective waters: while the densest water masses are formed in the deep convection areas (interior), eddies are responsible for along-isopycnal steering of these dense water masses into the boundary current before exiting the marginal sea (Brüggemann & Katsman, 2019).

It is expected that reducing the density difference between interior and the boundary current leads to a weakening of the current. A less pronounced density front between the warm boundary current and the cold interior makes the boundary current less susceptible to baroclinic instability along the topographic narrowing at West-Greenland. The decrease in this buoyant source could possibly result in less frequent and intense eddy fluxes that are responsible for bringing buoyant water into the interior. Simultaneously, this could have an immediate impact on the export routes for convected waters, as the same eddies are able to steer these waters into different preferred directions. Consequently, the response time of variability in the LSW production will differ, so does the strength of the AMOC. For example the reduction in density difference between interior and boundary current may allow the water mass transformation of dense water masses to exit more directly instead of an indirect route towards the topographic narrowing, as a result of matching boundary-interior densities at depth.

Besides its routes, it is expected that a reduced eddy activity yields denser waters, as less buoyant water is brought into the interior. In combination with a reduced eddy-exchange mechanism at the boundary current-interior, residence times of convective waters are likely to increase. Alternatively, a weakened eddy field may lead to less restratification of surface waters, thereby possibly opening the export route

of lighter water masses at the West-Greenland coast. The opposite holds for a strengthening of the eddy field. Beforehand, it is not clear what the net effect will be. Georgiou et al. (2019) already concluded that some changes in the forcing conditions are not simply proportional to changes in the eddy field and thus scale non-linearly with the properties of convection. This emphasis the necessity for further investigation of changes in the properties of the boundary current for both the product of convection, its export pathways and the associated timescales.

1.3. Aim of study

The aim of this study is to provide qualitative insight on the effects of variations in boundary current strength on export pathways of convective water masses in the Labrador Sea. Since entrainment can only take place at locations and depths where both density and depth match the local water mass properties of the boundary current (Georgiou, et al., 2021), this study intends to test the hypothesis that the density structure of the boundary current is the dominant process controlling these locations and depths where the LSW can exit the interior. As the interior-boundary current exchange is crucial for export pathways and associated timescales of the LSW, the study aims to provide better understanding on this process and the variability therein, which is needed to understand the linkage between Labrador Sea dynamics and AMOC variability.

1.4. Approach

This study uses the same idealized model as Georgiou et al. (2019). Numerical model simulations will be set-up with different scenarios of the density structure of the boundary current at the inflow location (southern tip of Greenland), respectively a 5% weakening and 5% strengthening with respect to the reference simulation used in Georgiou et al. (2019). This is done by adjusting the analytical expression (in Chapter 2) for the temperature structure (and indirectly the density structure), which was first presented by Katsman et al. (2004), and later used by Gelderloos et al. (2011) and Georgiou et al. (2019). In Chapter 3 the different scenarios are introduced and a comparison is made of the Labrador Sea dynamics for each scenario with respect to the reference simulation. The output of the different simulations is compared on the basis of main features (e.g. barotropic streamfunction, mixed layer depth (MLD), eddy kinetic energy (EKE) and potential vorticity). In Chapter 4, a passive tracer is released in the basin, among which the convection area. The tracer analysis provides a qualitative description of the connection between the interior and boundary current, and reveals export pathways. This approach is similar to the tracer analyses performed by Brüggemann and Katsman (2019) (idealized model of generic marginal sea) and Georgiou et al. (2019) (idealized model of the Labrador Sea). Eventually, Chapter 5 provides a conclusion and discussion.

CHAPTER 2

MODEL SET-UP

This chapter introduces the idealized numerical model used in Georgiou et al. (2019), the adjustments made to the forcing conditions, and the set-up of scenarios.

2.1. Model configuration

The numerical simulations described in this study are performed with the Massachusetts Institute of Technology General Circulation Model (MITgcm) (Marshall, et al., 1997). MITgcm is based on the incompressible Navier Stokes equations and is designed for studies of the ocean circulation on global scales, where the horizontal scale of the motion becomes much larger than the vertical scale (e.g. hydrostatic pressure assumption can be applied in the vertical direction for the momentum equation) and on horizontal scales that are less than the depth of the ocean (e.g. non-hydrostatic pressure field). Physically motivated preconditioners are used to switch from hydrostatic to non-hydrostatic limit, allowing the model to address a wide range of scales and phenomena (Marshall, et al., 1997), from deep ocean convection on the left of Figure 2.1 to global circulation patterns on the right [1].

Based on MITgcm, an idealized eddy-resolving regional model for the Labrador Sea is used, similar to Georgiou et al. (2019). This is an improved version of idealized Labrador Sea models used in Katsman et al. (2004) and Gelderloos et al. (2011) in terms of resolution (horizontal and vertical), and by inclusion of seasonal variations of both the inflow boundary current and surface forcing.

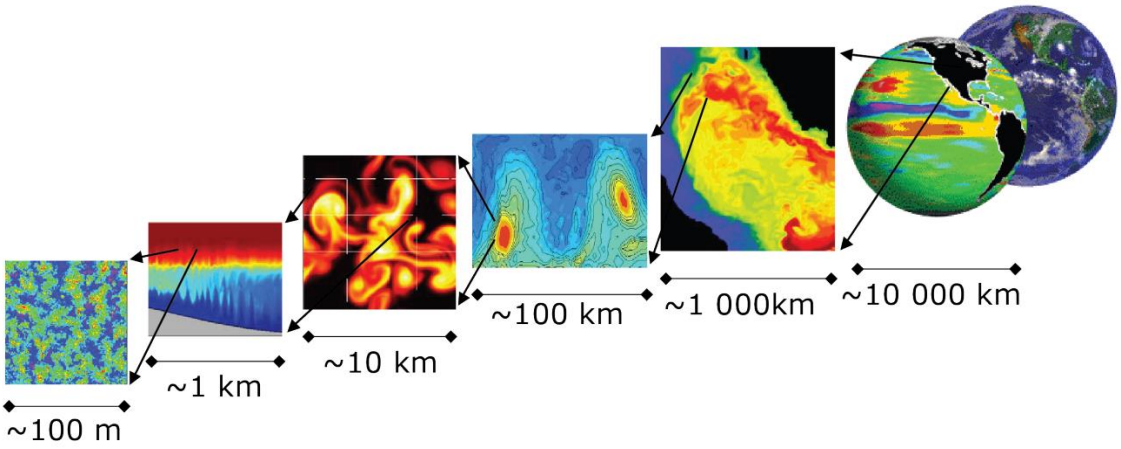

Figure 2.1 Non-hydrostatic capabilities of MITgcm allow the applicability of a wide range of scales and ocean phenomena. From: MITgcm Documentation (2021).

The model domain has the following dimensions: 1575 km in the meridional direction and 1215 km in the zonal direction. The horizontal resolution in both x and y is 3.75 km (Cartesian coordinates). In the vertical 40 layers are distinguished with a resolution of 20 m in the upper layers up to 200 m near the bottom. The maximum depth is 3000 m. Along the boundaries of the basin a continental slope is

[1] Following Georgiou et al. (2019), the non-hydrostatic possibility is switched off as resolving the small-scale features of deep convection is numerically expensive. To this end, deep convection is parameterized by an enhanced vertical diffusivity coefficient, once unstable conditions occur (i.e. when the surface layers get denser than the deeper layers).

present and at the West-Greenland coast the topographic narrowing is applied. The steepening of this slope is crucial for shedding the Irminger Rings (IRs) from the boundary current (Katsman, et al., 2004). The shelves have been omitted for simplicity.

The model domain has two open boundaries: the boundary current enters in the northeast and exits in the southwest of the domain (black arrows in Figure 2.2a). The inflow boundary current in the northeast is prescribed by a meridional temperature field $T_{ini}(y,z)$ and the associated shear velocity $\mathbf{U}_{ini}(y,z)$ [2] (Figure 2.2b), which follows from the thermal wind balance. In the model, salinity variations are omitted, such that density depends on temperature only. Seasonal temperature variations are superimposed by a sinusoidal term. Details on the derivation and choice of initial parameters of the inflow boundary current are provided in Section 2.2. At the outflow an Orlanski radiation condition is applied to all variables (which is a modified Sommerfeld radiation condition for more complex hyperbolic flows). Consequently, the properties of the boundary current exiting the domain are determined by the internal model dynamics (Georgiou, et al., 2019). All other boundaries are closed. Therefore, possible interactions with the Arctic via the Davis Strait are neglected, as well as any exchange of water masses with the North Atlantic via the interior of the Labrador Sea, and fresh water release from melting sea-ice and discharge of the Greenland continental ice sheet. Figure 2.2 shows a snapshot of the model domain and the prescribed temperature and velocity field at inflow.

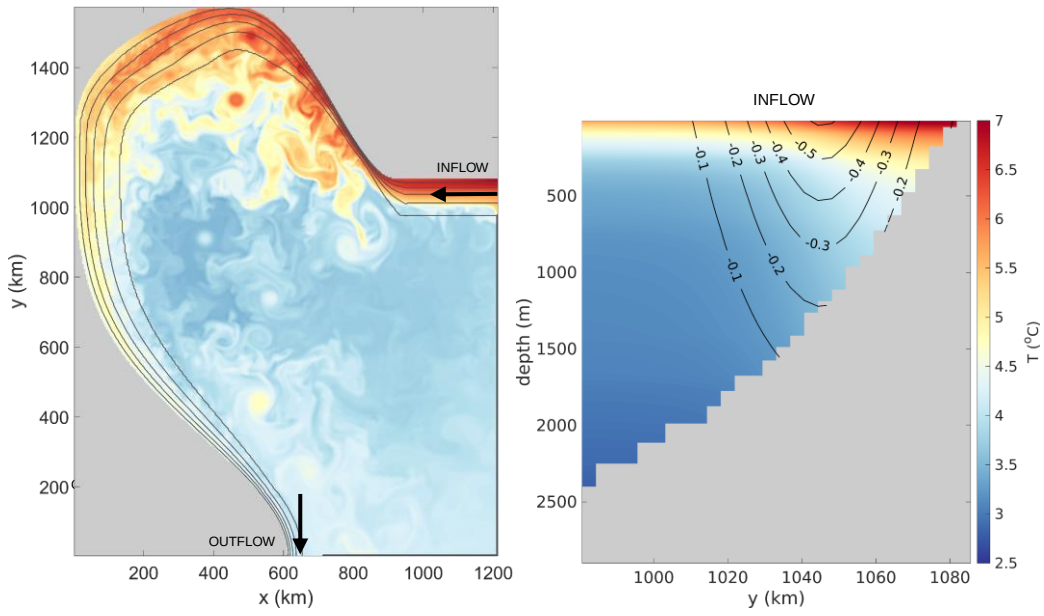

(a) (b)

Figure 2.2 (a) Snapshot of the model domain for the sea surface temperature (SST in ℃) for the reference simulation at mid-April just after wintertime convection of model year 16. Black contours are isobaths with contour interval of $500\ m$ starting from the first isobath of $500\ m$. The grey area is the simplified bathymetry of the Labrador Sea. The black arrows indicate the inflow/outflow. (b) Cross-section of inflow region showing the annual mean temperature field ($T_{ini}(y,z)$ in ℃) and zonal velocity ($\mathbf{U}_{ini}(y,z)$ in m/s, black contours)

The eddy-resolving model of Georgiou et al. (2019) requires a turbulent closure model that accounts for the subgrid-scale effects i.e. only the largest scales of motion are resolved; the smaller scales are parameterized. A key goal is to allow dynamics at the resolved scales to dominate the sub-grid

[2] In this report vectors are denoted with bold font.

parametrization, which implies that hydrodynamic instabilities and turbulence is not handicapped by strong frictional dissipation of momentum (Griffies & Hallberg, 2000). This permits mesoscale eddies in large-scale ocean modelling. Griffies and Hallberg (2000) proposed a closure model for eddy-permitting ocean models: a Smagorinsky-like viscosity with a biharmonic operator. The biharmonic operator allows friction to preserve numerical stability without affecting the resolved scales severely. Using a harmonic form of friction instead would remove too much kinetic energy over a wide range of spatial scales. In the end, the turbulence model approximates the eddy viscosity (and indirectly the eddy diffusivity), which closes the equations of motions. The exact values of these parameters are listed in Table 2.1.

Furthermore, the linear bottom drag coefficient reads $2 \cdot 10^{-4}\ m/s$. In addition, given the size of the domain, the β-plane approximation is used which allows the Coriolis parameter to vary linearly with latitude. This is a first-order Taylor expansion:

$$f \approx 2\Omega \sin(\varphi_a) + \beta \mathrm{R}(\varphi - \varphi_a) = f_0 + \beta y \qquad [2.1]$$

With:

$$\beta = \frac{\mathrm{d}}{\mathrm{d}y} 2\Omega \sin(\varphi) = \frac{\mathrm{d}}{\mathrm{d}y} 2\Omega \sin(y/\mathrm{R} + \varphi_a) = \frac{2\Omega \cos(\varphi)}{\mathrm{R}} \qquad [2.2]$$

Where f is the Coriolis parameter $[s^{-1}]$, the β-parameter $[m^{-1}s^{-1}]$, $\Omega = 7.29 \cdot 10^{-5}$ rad$/s$ the angular velocity of Earth's rotation, R distance of the water body to the center of the Earth $[m]$, φ the degree latitude and φ_a the average latitude of the domain. The values used are $f_0 = 1.16 \cdot 10^{-4}\ s^{-1}$ and $\beta = 1.4 \cdot 10^{-11}\ m^{-1}s^{-1}$.

Parameter	Symbol	Value	Unit
horizontal eddy viscosity (biharmonic)	A_h	$0.25 \cdot 10^9$	m^4/s
vertical eddy viscosity (harmonic)	A_v	$1.0 \cdot 10^{-5}$	m^2/s
horizontal eddy diffusivity (biharmonic)	K_h	$0.125 \cdot 10^9$	m^4/s
vertical eddy diffusivity (harmonic) [3]	$\mathrm{K}_v(z)$	$\mathrm{K}_b + \mathrm{K}_0 \mathrm{e}^{(-z/z_b)}$	m^2/s
	K_b	$1.0 \cdot 10^{-5}$	m^2/s
	K_0	$1.0 \cdot 10^{-3}$	m^2/s
	z_b	100	m

Table 2.1 Parameters used in turbulence closure model of Georgiou et al. (2019)

Georgiou et al. (2019) follows Katsman et al. (2004) for the initialization of the stratified layers $\rho_{ref}(z)$ (reference density), making use of hydrographic information along the WOCE AR7W section (World Ocean Circulation Experiment). The initial density profile is taken spatially uniform across the layers for simplicity. The model reaches a quasi-equilibrium state for the average temperature of the basin. This time is referred to as the model's spin-up time, and depends on the initial and boundary conditions set at start. For example, Georgiou et al. (2019) required a spin-up time of 15 years for the reference simulation, and use the years 15 till 20 for the analysis. In Chapter 3 it will be shown that the spin-up

[3] Note that the vertical eddy diffusivity decays exponentially with increasing depth in order to mimic the vertical mixing caused by winds (Woud, 2020) (because wind forcing is absent in the model). In case of statically unstable conditions (i.e. when $\partial\rho/\partial z > 0$), enhanced vertical diffusivity is applied to the convection process ($\mathrm{K}_v = 10\ m^2/s$) (Georgiou, et al., 2019).

time is sensitive to changes in the density structure of the inflow boundary current, (non)-favouring the spin-up time.

In this idealized model only the influence of temperature is considered, neglecting the role of salinity for simplicity. This can be justified because in the Labrador Sea the density changes are dominated by variations in temperature (Gelderloos, et al., 2011), and since we are only interested in the underlying dynamics of downwelling in response to changing boundary conditions. This implies that solely a vertical temperature gradient $\mathrm{T}(z)$ represents the initial stratification.

Using a linear equation of state the reference density is calculated as follows (Katsman, et al., 2004):

$$\rho_{ref}(z) = \rho_0[1 - \alpha\Delta\mathrm{T}] = \rho_0\left[1 - \alpha\left(\mathrm{T}_{ref}(z) - \mathrm{T}_0\right)\right] \quad [2.3]$$

Where $\rho_{ref}(z)$ is reference density per layer depth $[kg/m^3]$, $\rho_0 = 1028\,kg/m^3$, the thermal expansion coefficient $\alpha = 1.7 \cdot 10^{-4}\ ℃^{-1}$, $\mathrm{T}_{ref}(z)$ is the temperature in [℃] per layer from the hydrographic section WOCE AR7W, and $\mathrm{T}_0 = 2.63$ ℃ the reference temperature at maximum depth. The temperature profile and calculated reference density profile (using Eq. [2.3]) are plotted in Figure 2.3.

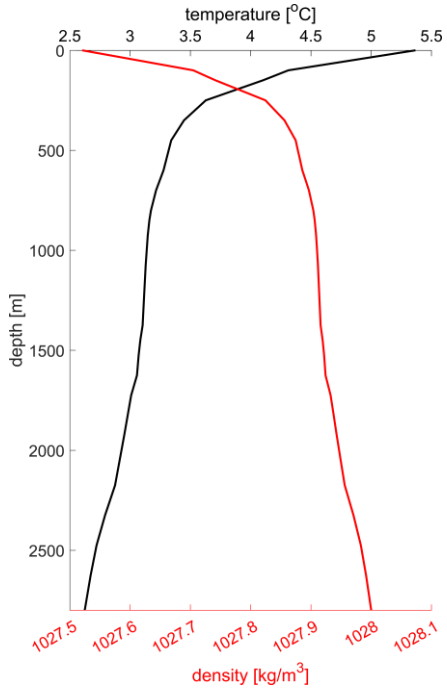

Figure 2.3 Temperature profile $\mathrm{T}(z)$ and density profile $\rho_{ref}(z)$, representative of the stratification in the western Labrador Sea, late summer (from WOCE AR7W).

2.2. Model forcing

The model is forced by a temporally and spatially varying surface heat flux (Figure 2.4b) together with a temporally varying inflow conditions at the eastern open boundary of the domain (Figure 2.2), which represents the West Greenland Current (WGC, Figure 1.2).

The surface heat flux is a spatially idealized version of the WHOI OAFlux project (Yu et al. 2008, Figure 2.4). The maximum heat loss occurs in the northwest and decays linearly from the elliptical-shaped field. The heat flux varies annually from $\mathcal{H} = -320\ W/m^2$ in January to $\mathcal{H} = 140\ W/m^2$ in July (solid

line). The dashed line in Figure 2.4c represents the mean over the basin for the reference run in Georgiou et al. (2019), with a net heat loss over the basin of $\langle \bar{\mathcal{H}} \rangle = -18\ W/m^2$.

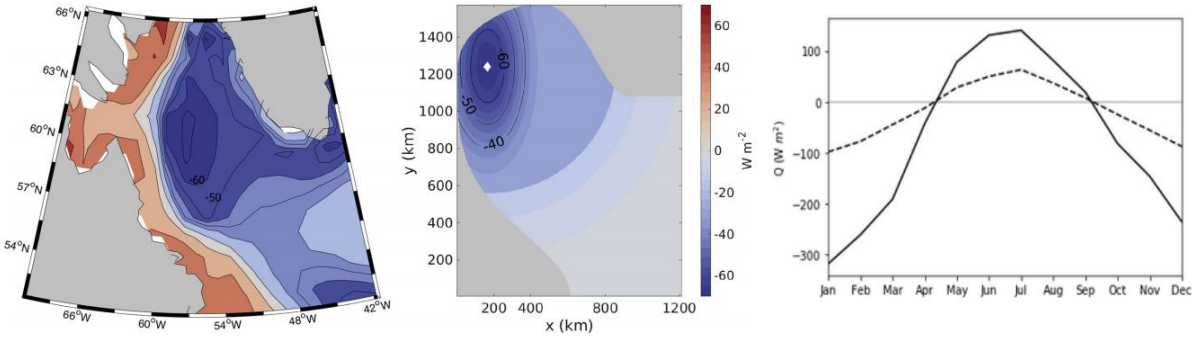

(a) (b) (c)

Figure 2.4 (a) Surface mean heat flux from WHOI OAFlux project (Yu, et al., 2008). (b) Annual mean surface heat flux $\langle \mathcal{H} \rangle$. From Georgiou et al. (2019) (c) Seasonal cycle of the amplitude of the surface flux at the location where the variation in amplitude is largest (at white marker in (b)) (solid line) and average surface heat flux over the basin $\bar{\mathcal{H}}$ (dashed line). From Georgiou et al. (2019).

As mentioned in section 1.2 the strength of the boundary current is prescribed by the horizontal density gradient between the buoyant boundary current and the denser interior. From the linear equation of state (which in this model only depends on temperature variations) it follows that the boundary current strength is determined by the meridional temperature field $\mathrm{T}_{ini}(y,z)$ in geostrophic balance with a westward flow $\mathbf{U}_{ini}(y,z)$. Following Katsman et al. (2004) we are using an analytical expression for the initial temperature section, which is defined as:

$$\mathrm{T}_{ini}(y,z) = \mathrm{T}_{ref}(z) - \frac{\Delta\rho}{2\alpha\rho_0}\left(1 - \frac{z}{z_b}\right)\left[1 + \tanh\left(\frac{y - y_0}{\mathrm{L}_y}\right)\right] \quad [2.4]$$

and

$$\mathbf{U}_{ini}(y,z) = -\frac{g\Delta\rho}{4f\rho_0\mathrm{L}_y}\frac{1}{\cosh^2\left(\frac{y - y_0}{\mathrm{L}_y}\right)}\frac{(z - z_b)^2}{z_b} \quad [2.5]$$

Where $\Delta\rho = -0.245\ kg/m^3$ is the density difference across the boundary current, $z_b\ [m]$ is the depth at which the velocity is zero $\mathbf{U}_{ini}(y,z_b) = 0$ (no slip condition), $y_0 = 22.5\ km$ is the location south of the tip of Greenland, $\mathrm{L}_y = 22.5\ km$ is the width of the inflowing boundary current, $f = 1.26 \cdot 10^{-4}\ s^{-1}$ is the Coriolis parameter according to Eq. [2.1], $g = 9.81\ m/s^2$ is the gravitational acceleration. $\mathrm{T}_{ref}(z)$ is the temperature profile of the interior in [°C] (from the hydrographic observations WOCE AR7W). The initial temperature profile at the inflow in Eq. [2.4] was proposed by Katsman et al. (2004) and decays linearly with depth and has a hyperbolic tangent relation from interior to the coast. The velocity profile in Eq. [2.5] follows from substitution of the linear equation of state into the thermal wind balance. A detailed derivation is given in Appendix A.

This expression has proven to be successful in earlier studies by Gelderloos et al. (2011) and Georgiou et al. (2019; 2020) capturing the key dynamics of the Labrador Sea, like the annual cycle of convection,

the process and timescales of restratification, and properties of the mesoscale eddy field. The seasonal component $T_{seas}(t,y,z)$ was added to the temperature field (Gelderloos, et al., 2011; Georgiou, et al., 2019):

$$T(t,y,z) = T_{ini}(y,z) + T_{seas}(t,y,z) \quad [2.6]$$

With $T_{seas}(t,y,z)$ defined as:

$$T_{seas}(t,y,z) = \Delta T_{int} + \frac{1}{2}(\Delta T_{WGC} - \Delta T_{int})\left[1 + \tanh\left(\frac{y-y_0}{L_y}\right)\right] e^{z/200}\left[1 + \sin\left(\frac{2\pi(t-6)}{12}\right)\right] \quad [2.7]$$

Where $\Delta T_{int} = 0.35$ ℃ and $\Delta T_{WGC} = 0.55$ ℃ are the seasonal temperature variations of the interior and the boundary current, respectively, and decays exponentially over the upper $200\ m$. t is time expressed in months (starting from January) and varies sinusoidally over time with a period of one year. The minimum values occur in late wintertime (March) and the maximum values occur in September. Note that the seasonal component $T_{seas}(t,y,z)$ in Eq. [2.6] will always add more buoyant water to the boundary current. Only in March the seasonal component of Eq. [2.7] is zero. The addition of ΔT_{int}, the first term on the right-hand side of Eq. [2.7], is required to have a positive inflow at all times, and thus numerically stable boundary condition (in case wind forcing is excluded).

2.3. Model scenarios

In this study, we aim in identifying changes in export pathways and associated timescales of convected waters due to variations in the boundary current strength. Towards this goal, we performed a reference simulation and two additional simulations in which the boundary current is altered by $\pm 5\%$ from the reference run in Georgiou et al. (2019), by changing the density difference $\Delta\rho$ between the interior and the boundary current in Eq. [2.4]. This means that the buoyancy of the inflowing waters are also changed. The model appeared to be highly sensitive to changes in this parameter, resulting in 'crashing' simulations in early stages. With a $\pm 5\%$ difference in $\Delta\rho$ it was possible to get a long simulation (15-20 years). This timescale is required for appropriate multi-year analysis as it takes approximately 15 years for the model to reach quasi-equilibrium. The model scenarios are listed below, including the density change $\Delta\rho$ and associated maximum change in surface velocity $\Delta\mathbf{U}$ (Table 2.2):

1. **Reference simulation (REF)**:
   following Georgiou et al. (2019)
2. **Weakened inflow boundary current (WEAK)**:
   5% weakening of the boundary current compared to REF
3. **Strengthened inflow boundary current (STRONG)**:
   5% strengthening of the boundary current compared to REF

The cross-section of the inflow, showing the annual mean temperature anomalies ($\Delta T_{ini}(y,z)$ in ℃) and zonal velocity anomalies ($\Delta\mathbf{U}_{ini}(y,z)$ in m/s) per model scenario, is given in Figure 2.5. These temperature and velocity profiles are deviations from the reference profile in Figure 2.2b. Changes of the maximum surface velocity ($\Delta\mathbf{U}_{ini} = \pm 0.3\ cm/s$, Table 2.2) are in the order of interannual variability of the geostrophic surface velocity in the Labrador Sea, derived from hydrographic data combined with AVISO satellite altimetry data (Rykova, et al., 2015). The anomaly plots in Figure 2.5 reveal the effect on the flow velocity due to variations in the density structure of the inflow conditions.

According to the thermal wind balance, a smaller (larger) horizontal density gradient will weaken (strengthen) the boundary current at inflow.

Model scenario	$\Delta\rho\ [kg/m^3]$	$\mathbf{\Delta U}\ [m/s]$ (max. surface velocity change)	Compared to REF in Georgiou et al. (2019)
WEAK	-0.23275	-0.0296	5% weakening
REF	-0.245	-	-
STRONG	-0.25725	+0.0296	5% strengthening

Table 2.2 Density difference across the boundary current $\Delta\rho$ in Eq. [2.4] per model simulation. REF value is from Georgiou et al. (2019).

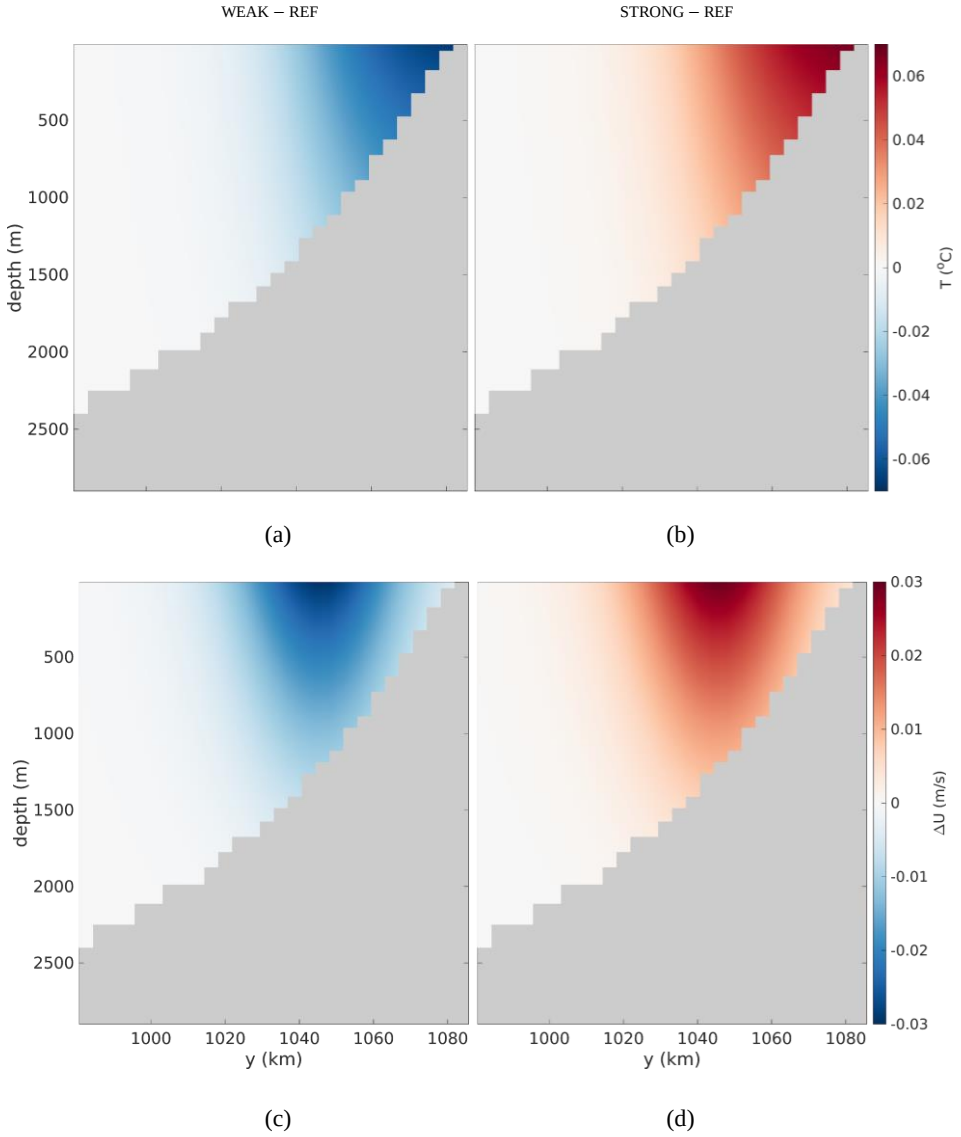

Figure 2.5 Cross-sections of inflow region showing anomalies of the annual-mean (a)-(b) temperature ($\Delta T_{ini}(y,z)$ in ℃) and (c)-(d) zonal velocity ($\mathbf{\Delta U}_{ini}(y,z)$ in m/s). The temperature field and associated velocity contours of REF are given in Figure 2.2b. Blue color indicates a colder, slower boundary current, in (a) and (c), respectively. Red color indicates a warmer, faster boundary current, in (b) and (d), respectively.

According to Eq. [2.6], the temperature field represented $T(t,y,z)$ in Figure 2.5 is a superposition of a time-invariant temperature field $T_{ini}(y,z)$ and the time-dependent seasonal component $T_{seas}(t,y,z)$.

Therefore, the effect of changing the time-invariant temperature field $T_{ini}(y,z)$ results in a transformed temperature field $T(t,y,z)$ with a shifted annual cycle. The mean over inflow section $\overline{T}(t)$ is plotted in Figure 2.6.

In the model, a year is defined as 12 months with 30 days for simplicity. All the simulations ran for a period of 20 years. After approximately 10-15 years, the simulations reach a quasi-equilibrium state considering the basin-mean temperature (see Figure 2.7). For the last five years of the simulation (i.e. years 16 to 20), two-day snapshots of the velocity vectors $\mathbf{U}(x,y,z)$ and the temperature scalar $T(x,y,z)$ were stored. Using the linear equation of state, the density $\rho(x,y,z)$ can be calculated easily for post-processing purposes. These diagnostics of the last five years are used for our analysis in Chapters 3 and 4.

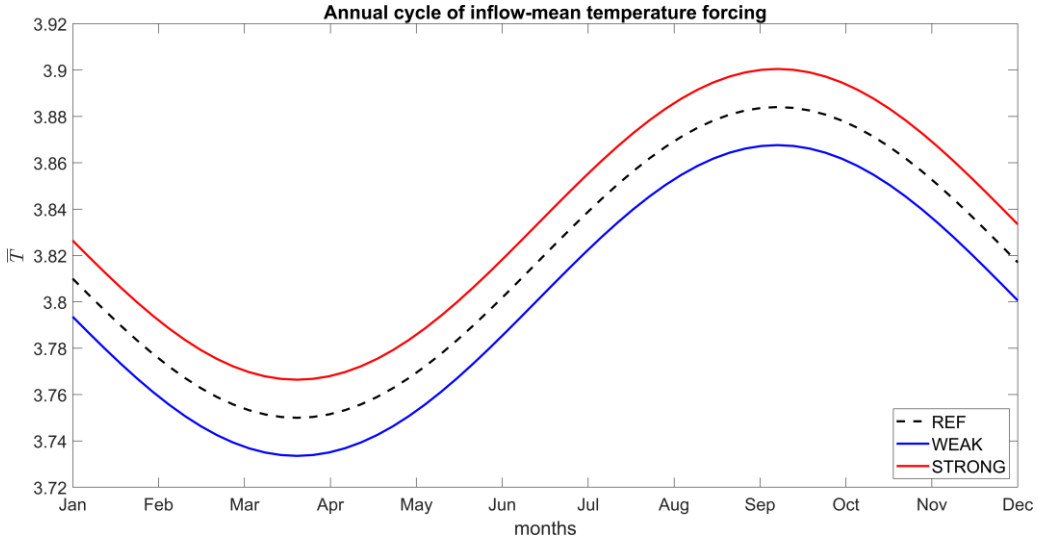

Figure 2.6 Annual cycle of the mean temperature forcing $\overline{T}(t)$ at the inflow section (see Figure 2.5) for all simulations.

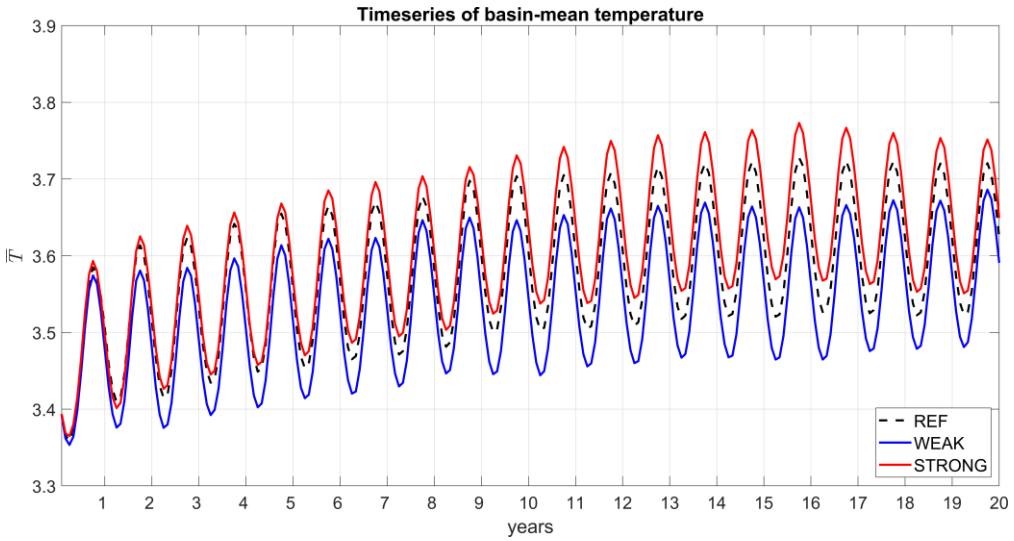

Figure 2.7 Timeseries of the basin-mean temperature $\overline{T}(t)$ in ℃ for all simulations.

According to Straneo (2006) and Spall (2012), the quasi-equilibrium state, represented in Figure 2.7, can only be reached by lateral advection of heat, compensating the surface heat loss over the boundary current as well as over the interior. Georgiou et al. (2019) confirmed that the idealized eddy-resolving model can reproduce this heat budget balance (Figure 2.8). The lateral heat advection can be decomposed into two components: the mean heat advection $\nabla \cdot (\overline{\mathbf{U}}\overline{\mathrm{T}})$ and the eddy heat advection $\nabla \cdot \left(\overline{\mathbf{U}'\mathrm{T}'}\right)$. Georgiou et al. (2019) assumed that those contributions mostly cancel each other (while the total heat advection efficiently balances the surface loss due to cooling (Figure 2.8)). Figure 2.9 shows the mean heat advection for each simulation.

Georgiou et al. (2019) noted that the mean heat advection governs the transport in the boundary current, while the eddy heat advection dominates the heat transport from the boundary to the interior, resulting in a warming of the interior. The negative contribution to the mean can be conceived as a preferred path for eddies, once detached from the boundary current. Along that path they cool and decay (in line with thermal wind balance). While the incoming boundary current transports a vast amount of heat into the marginal sea, gradients in the mean heat transport start as soon the current reaches the topographic narrowing along the West-Greenland coast. For STRONG the positive contribution is more confined to the coast compared to REF and WEAK. This stems from a larger density difference across the boundary current in STRONG, leading to faster northward-flowing current (according to thermal wind balance). Later, in Chapter 3 we will analyze the barotropic streamfunction (Ψ_b), which corroborates that the streamlines are located closer for STRONG than for REF and WEAK, respectively. In those last two scenarios the advection of heat is more constricted to the boundary current and reaches farther downstream. In STRONG eddies detach more downstream and travel farther into the interior on average. This suggests eddies that maintain their density gradients longer, which is the potential energy source for these vortices. For WEAK eddies detach more upstream. Possibly, for WEAK, eddies might detach from the boundary current easier, while for STRONG eddies might stay within the regime of the faster boundary current. This could be verified by further weakening/strengthening of the boundary current or by minor changes in the bathymetry and see whether this principle still holds. This is however outside the scope of the study.

As obtained from Figure 2.7 all simulations come to an equilibrium, and because the basin-mean temperature does not deviate much between the scenarios, the differences in lateral heat advection are small as well (especially for the heat advection in the boundary current). Though, slight changes to the boundary current already induce a significant change in locations where eddies detach from the boundary current and what their preferred path is when moving towards the interior.

From the above and earlier studies with this idealized model (Gelderloos, et al., 2011; Georgiou, et al., 2019), it becomes clear that by resolving the mesoscale eddies the model is able to mimic the lateral heat advection required for a quasi-equilibrium state of the basin. This study shows that under changing boundary conditions this equilibrium is still valid. And according to Georgiou et al. (2019) it is considered appropriate for further analyze of the Labrador Sea dynamics, in particular the process of deep convection and downwelling. These processes are thought to be of paramount importance for the type of water masses formed, their formation location (lateral and depth), and their pathway towards exiting the interior.

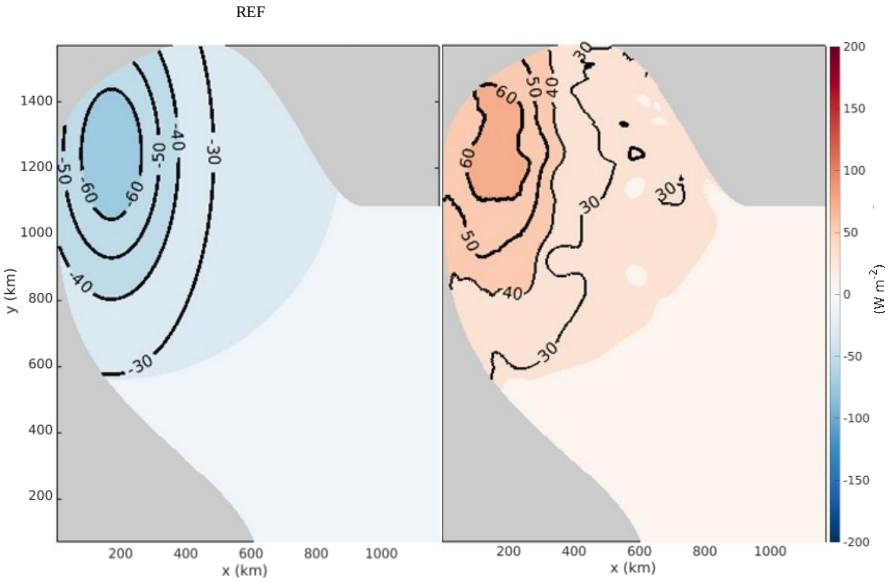

(a) (b)

Figure 2.8 (a) Surface heat flux $\langle \mathcal{H} \rangle$ (average over years 16-20). (b) Depth-integrated total heat advection for REF: $total\ heat\ advection = mean\ heat\ advection + eddy\ heat\ advection = \nabla \cdot (\overline{\mathbf{U}}\,\overline{\mathrm{T}}) + \nabla \cdot (\overline{\mathbf{U}'\mathrm{T}'})$. Overbars denote the five year means, primes denote the anomalies with respect to this mean. From Georgiou et al. (2019).

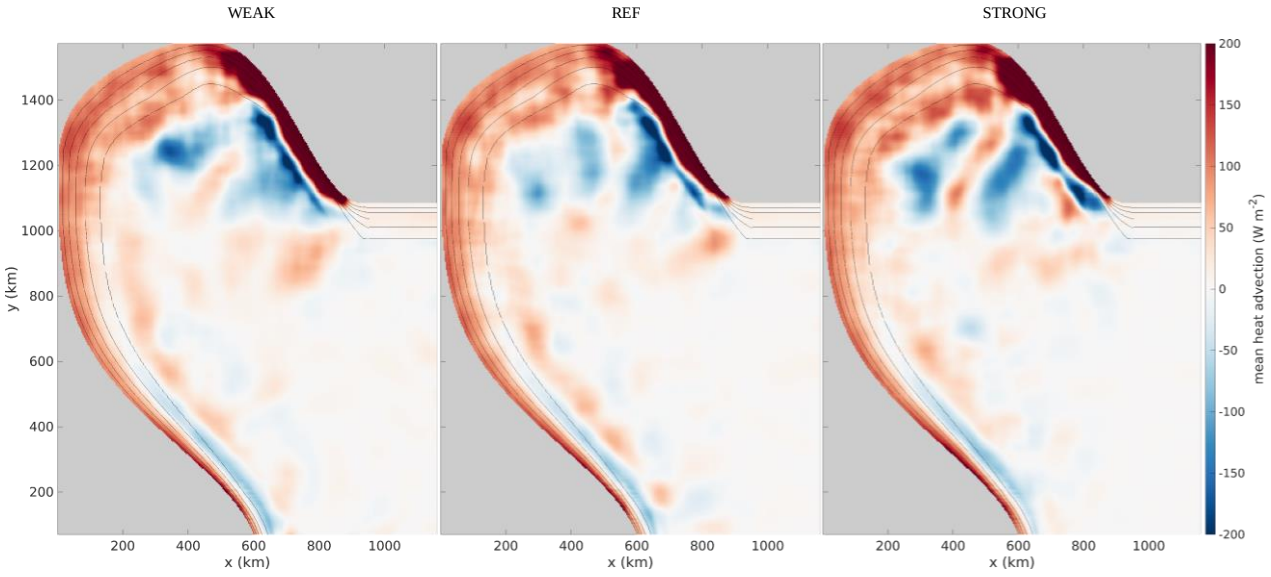

(a) (b) (c)

Figure 2.9 Depth-integrated mean heat advection $\nabla \cdot (\overline{\mathbf{U}}\,\overline{\mathrm{T}})$ for each simulation. Black contours are isobaths with contour interval of $500\ m$ starting from the first isobath of $500\ m$.

CHAPTER 3

MAIN FEATURES OF IDEALIZED LABRADOR SEA DYNAMICS

This chapter elaborates on the changes in Labrador Sea dynamics induced by variations in the boundary current strength.

3.1. Barotropization of the boundary current

In this study, we explore the pathways of convective waters that exit the Labrador Sea via the boundary current. More specifically, we analyse the role of the boundary current-interior interaction that controls the location and depth where entrainment can occur i.e. where both density and depth match the local water mass properties of the boundary current. To this end, we define the barotropic streamfunction Ψ_b such that $\mathbf{U} = \nabla \times \Psi_b$ which is equivalent to $u = \partial\psi/\partial y$ and $v = -\partial\psi/\partial x$ in a Cartesian coordinate system. The five-year mean streamlines are plotted in Figure 3.1, with a clear distinction between the boundary current and interior. At the topographic narrowing the streamlines of the boundary current contract, which indicates a faster-flowing current. For STRONG the streamlines are closer together than for REF and WEAK. The total transport that enters the basin is 18.7 Sv for WEAK, 19.7 Sv for REF, and 20.7 Sv for STRONG. Following Georgiou et al. (2020), we defined the 18 Sv contour line of the five-year mean barotropic streamfunction as the border between the boundary current and interior for REF (black dashed line in Figure 3.1). Consequently, the choice for distinguishing the boundary current from the interior for WEAK and STRONG is consistently cut off at 17 Sv and 19 Sv, respectively.

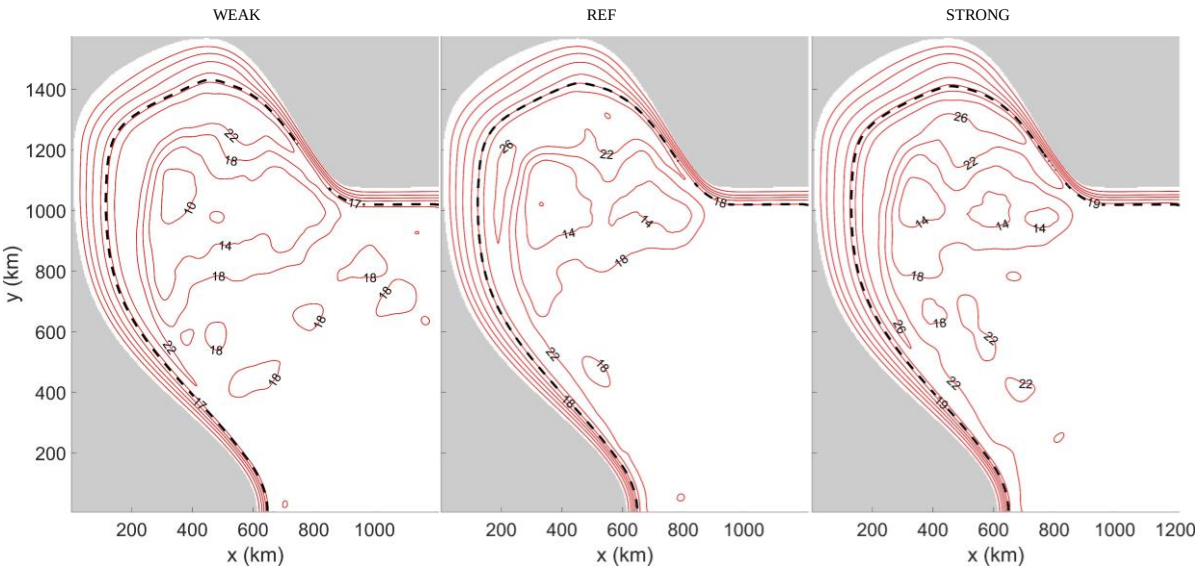

Figure 3.1 Five-year mean barotropic streamfunction (red contours; contour interval is 4 Sv). The black dashed line distinguishes the boundary current from the interior (WEAK: 17 Sv, REF: 18 Sv, STRONG 19 Sv).

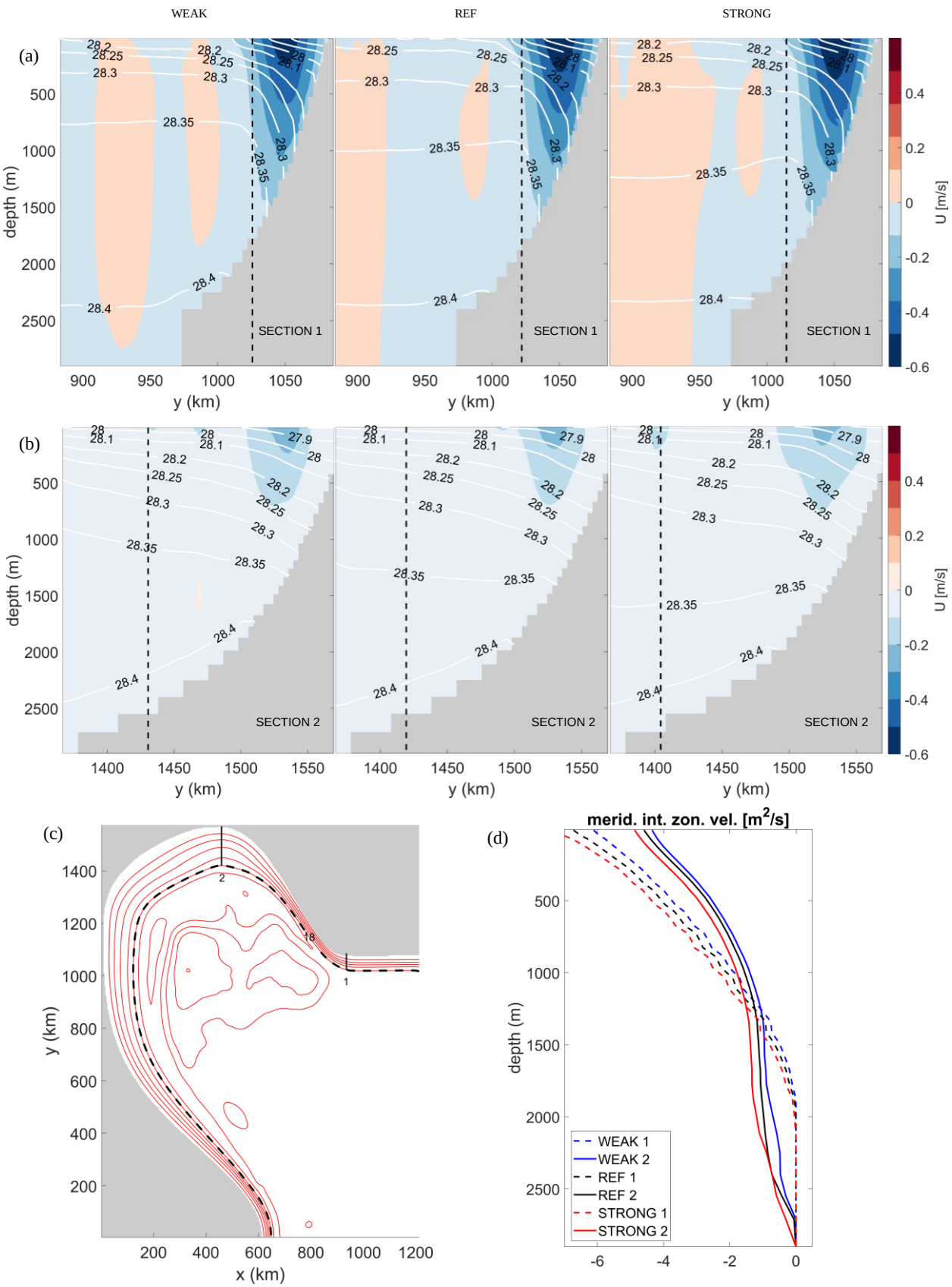

Figure 3.2 (a)-(b) Zonal velocities at sections 1 and 2, respectively. Density $\sigma = \rho - 1000$ (in kg/m^3) is indicated by white contour lines. The vertical dashed line denotes the location of the 17 Sv (WEAK), 18 Sv (REF), 19 Sv (STRONG), contour line. (c) Five-year mean barotropic streamfunction (similar to REF in Figure 3.1) including location of the sections. (d) Zonal velocities integrated meridionally over the width of the boundary current for each scenario and section in (a) and (b).

According to Spall (2004) and Straneo (2006), the definition of the barotropic streamfunction allows to define the total depth-integrated boundary current transport to be constant along its path, even though its width changes. This property enables us to assess the overturning in the boundary current, in particular the region with strong eddy activity (see Section 3.4). According to Brüggemann and Katsman (2019), the mechanism behind the overturning is due to surface heat loss (see Figure 2.8a) and/or lateral eddy fluxes. The latter is responsible for the advection of buoyant water from the boundary current to the interior at upper layers, while the same eddies laterally steer the densest waters along isopycnals from their formation location (interior) towards the boundary current (Brüggemann & Katsman, 2019). Consequently, the boundary current becomes denser along its path. The density difference between the boundary current and interior reduces, and therewith the thermal wind shear decreases. The boundary current decelerates in upper layers while accelerating in lower layers: the boundary current becomes more barotropic. According to Spall (2004) and Straneo (2006), the barotropization of the boundary current reflects the transfer of waters from the upper limb to the lower limb of the boundary current. However, this downward transfer is not established through diapycnal mixing but through an interplay of along-isopycnal flow at the current-interior section in which the mesoscale eddies play an important role (Brüggemann & Katsman, 2019).

In order to assess the overturning, we follow Brüggemann and Katsman (2019) in Figure 3.2. For each scenario, two cross-sections are plotted perpendicular to the boundary current flow. Barotropization of the boundary current is evident when comparing Figure 3.2a with Figure 3.2b: while the flow is sheared in section 1 (i.e. sloping isopycnals), density gradients have been reduced in section 2, therewith reducing its speed in upper layers. Figure 3.2d shows that indeed the transport in upper layers decreases while the transport increases at depth.

This confirms that overturning occurs along the narrowing for all simulations. The magnitudes of the meridionally integrated transport in Figure 3.2d are almost identical per scenario, when scaled to the width of the boundary current. This suggests that the overturning strength scales with the boundary current strength. And the larger the overturning volumes, the more dense water is entrained in the boundary current at deeper layers.

3.2. Eddy kinetic energy

To address the impact of the mesoscale eddies on the Labrador Sea dynamics, we calculate the intensity of the eddy field. Following Georgiou et al. (2019), the intensity is measured in terms of eddy kinetic energy (EKE):

$$\mathrm{EKE} = \frac{1}{2}\overline{(u'^2 + v'^2)} \qquad [3.1]$$

Where EKE is in $[m^2/s^2]$. In this expression, the velocity is decomposed in a mean component and a deviation from the mean motion (e.g. Reynolds decomposition): $u = \bar{u} + u'$. The overbar indicates the time-averaged flow and the primes are the deviations from this time-averaged flow. Figure 3.3a-c shows the five-year mean EKE for all three simulations, where the deviations u' and v' are based on the two-day snapshots.

The maximum EKE is found near the West-Greenland continental slope, where the boundary current is forced to narrow (becoming barotropically unstable). Maximum values are 705 cm^2/s^2 (WEAK), 625 cm^2/s^2 (REF), and 750 cm^2/s^2 (STRONG), respectively. So apparently, the strength of the boundary current is not proportional to the maximum intensity of the eddy field. A possible explanation

is that eddies in WEAK are more confined to the coast: they do not fully detach from the boundary current. This intensifies the EKE in the area close to the coast. In REF, eddies could detach more distinct from the boundary current as they carry more potential energy along with them. Consequently, they travel away from this area of high EKE at the coast and distribute their energy to the interior.

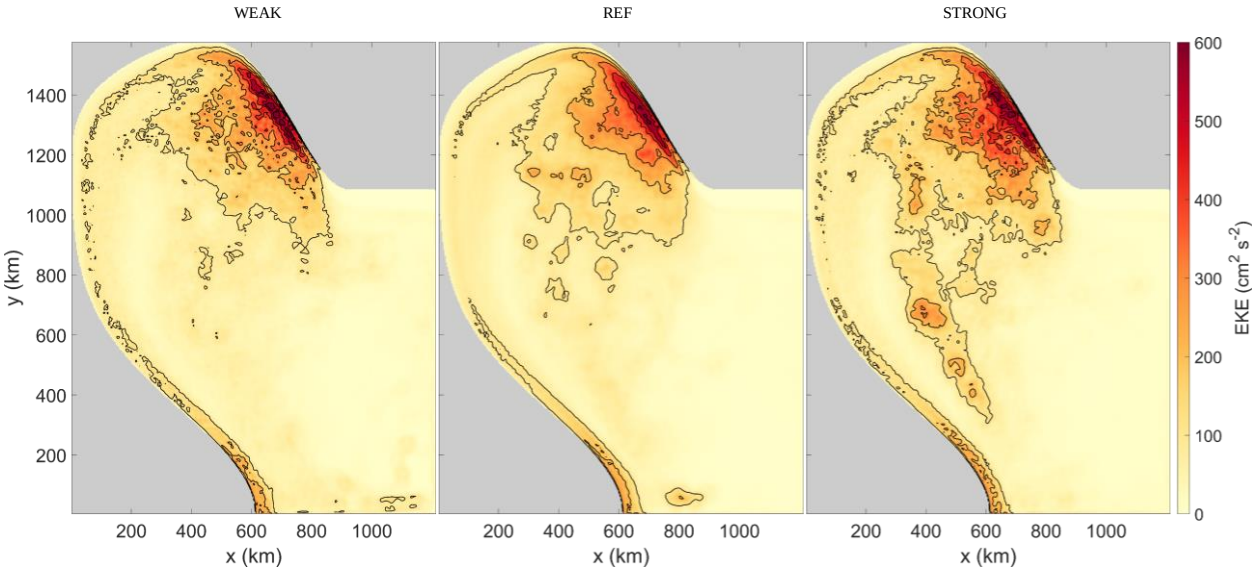

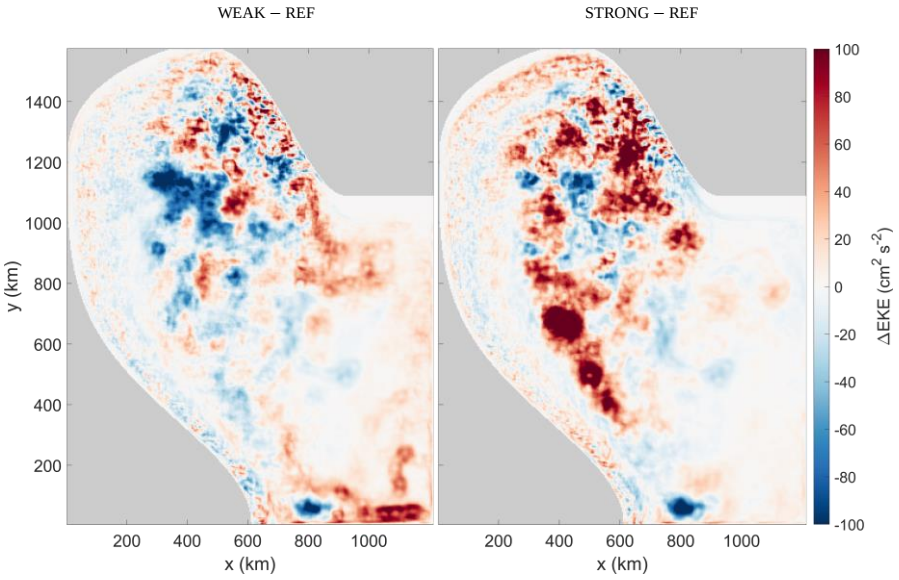

Figure 3.3 (a)-(c) Five-year mean surface eddy kinetic energy (EKE) (black contours; contour interval is 100 cm^2/s^2). (d)-(e) Anomalies of five-year mean surface eddy kinetic energy (EKE). Blue color indicates reduced EKE. Red color indicates increased EKE.

The EKE is higher (lower) in the interior for STRONG (WEAK) compared to REF (this becomes even more clear from the anomaly plot in Figure 3.3d-e). This suggests that eddies live longer and can travel

further into the interior with increasing baroclinicity of the boundary current. Consequently, the eddies transport more (less) buoyant water towards the interior for STRONG (WEAK) compared to REF. This has implications for the convection process. This will be further analysed in Sections 3.3 and 3.4.

3.3. Mixed layer depth

The mixed layer depth (MLD) can be thought the depth over which the water column is unstable. Following Katsman et al. (2004), the MLD is defined as the depth at which the temperature is lower than the surface temperature by $dT = 0.025$ ℃. Using the linear equation of state in Eq. [2.3], this temperature difference dT is equivalent to a change in density of $d\rho = 5 \times 10^{-3}\ kg/m^3$.

From Figure 3.4a-c it is evident that slight changes in the boundary current have a significant effect on the MLD. Note, these dynamic properties were established after the system has reached equilibrium (e.g. 10-15 years, Figure 2.7). The deepest convection is found in the south-western part of the marginal sea, reaching 1950 m (WEAK), 1700 m (REF) and 1450 m (STRONG), respectively. Georgiou et al. (2019) already noticed that the deepest mixed layers are not located where the surface heat loss is at maximum (compare with Figure 2.8a). Thus, under the same surface forcing, and with increasing baroclinic strength of the boundary current (i.e. STRONG), the MLD becomes shallower in depth and smaller in area. This is likely because eddies bring more buoyant water from the boundary current into the interior, effectively limiting the extent of convection.

Anomaly plots of the MLD (see Figure 3.4d-e) corroborate this way of reasoning. The anomalies for WEAK (with respect to REF) indicate an increased MLD at the western side of the interior. This suggests that less eddies are shed and/or less energetic eddies detach from the boundary current at the West-Greenland coast. They cannot make it far into the interior and decay faster compared to REF. The anomalies for STRONG (with respect to REF) indicate a decreased MLD at the centre/eastern-side of the interior. As expected, the higher eddy activity in STRONG prohibits deep convection significantly, as the restratification of the basin is more efficient. The changes in horizontal and vertical extent of the convection area are likely associated with changes in the properties of its product.

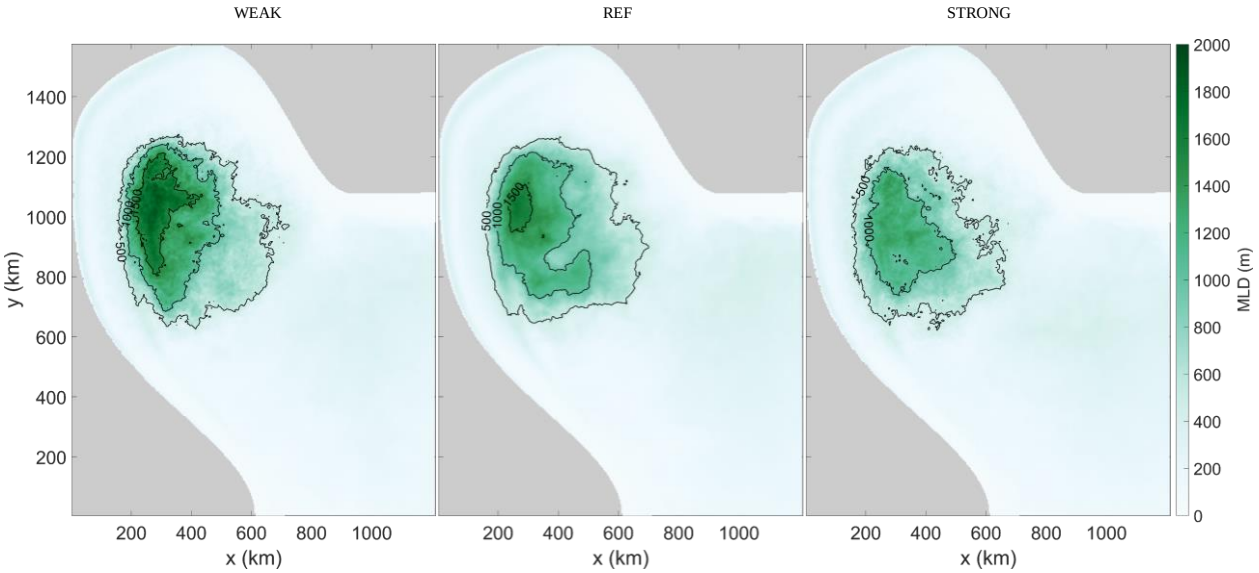

(a) (b) (c)

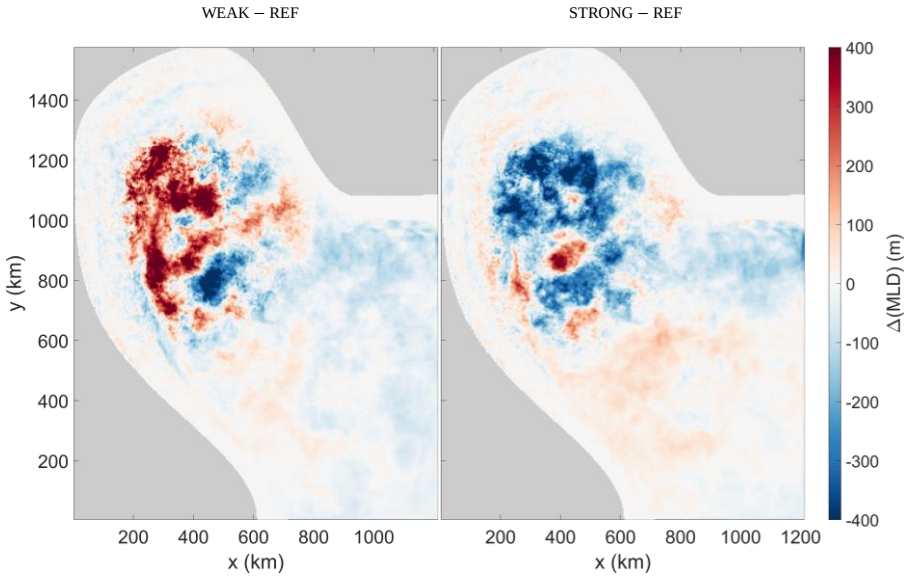

(d) (e)

Figure 3.4 (a)-(c) Five-year mean of the winter (February-March) mixed layer depth (MLD) (black contours; contour interval is $500\,m$). (d)-(e) Anomalies of five-year mean mixed layer depth (MLD) for wintertime (February-March). Blue color indicates shallower mixed layer. Red color indicates deeper mixed layer.

3.4. Properties of convected water

The differences in deep convection between the scenarios become obvious when studying hydrographic sections across the domain. Figure 3.5a shows the mean hydrographic section along the WOCE AR7W in late spring. Notably, the isopycnals of dense waters, in particular the $28.35\ kg/m^3$ – contour line ($\sigma = \rho - 1000$), differ significantly in the interior. In this region, the proportion of convected water

that is found between the isopycnals $28.35 - 28.40\ kg/m^3$ is smaller (larger) for STRONG (WEAK) compared to REF; the proportion between the isopycnals $28.30 - 28.35\ kg/m^3$ is larger (smaller) for STRONG (WEAK) compared to REF. This suggests that the product of convection is lighter (heavier) for STRONG (WEAK).

In order to properly define what the product of convection is per scenario, we determine the potential vorticity (PV) along the section. This is because convected waters are commonly defined as being weakly stratified in the vertical (Georgiou, 2021).

Following Talley and McCartney (1982), the potential vorticity PV $[(m\ s)^{-1}]$ is:

$$\mathrm{PV} = -\frac{f}{\rho}\frac{\partial \rho}{\partial z} \qquad [3.2]$$

Where f is the Coriolis parameter $[s^{-1}]$ determined with Eq. [2.1] and ρ is the density $[kg/m^3]$. Note that in this idealized model, density is based on temperature only.

Following Georgiou (2021), a threshold of $\mathrm{PV} < 4 \cdot 10^{-12}\ (m\ s)^{-1}$ is chosen for identification of the isopycnals that bound the convected water. Figure 3.5b shows the mean PV along the hydrographic section WOCE AR7W in late spring. Table 3.1 lists the isopycnals that define the convected water in each simulation.

Scenario	**Isopycnal limits** $\sigma = \rho - 1000\ [kg/m^3]$
WEAK	28.35 – 28.39
REF	28.34 – 28.38
STRONG	28.33 – 28.37

Table 3.1 Isopycnal limits of convected waters per scenario

The results of Table 3.1 suggest a negative correlation for the boundary current strength and the density of convected water masses formed in the interior. This is in line with the depth to which deep convection reaches (i.e. the MLD of each simulation, Figure 3.4), and earlier statements made about the volumetric weight of the dense water product and depth at which it is located.

Consequently, the convected waters formed in the interior are expected to follow a different (depth-)path prior to exiting the domain. This is based on the fact that the depth and the location at which the convected water masses will enter the boundary current strongly depends on the local properties of the boundary current and of the convected waters themselves (Georgiou, 2021). In addition to a lighter/denser product, pathways are likely to change as entrainment is governed by a match in density and depth between the boundary current and the interior. Once there is a match, the instantaneous eddy field (i.e. its strength and pattern, Figure 3.3) might impact the entrainment, as overturning volumes are likely to scale with the eddy activity close to the boundary current.

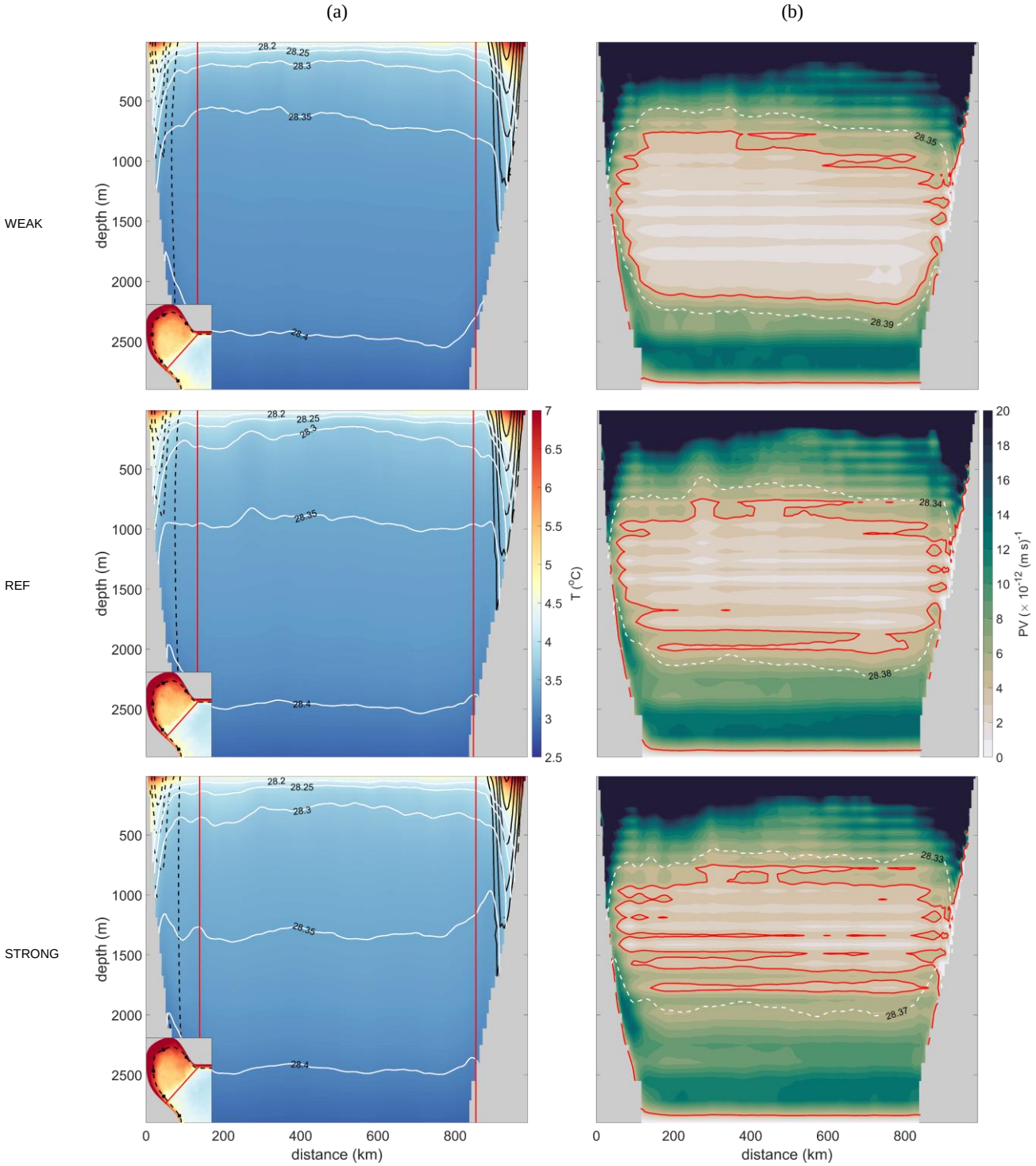

Figure 3.5 (a) Late spring (May-June) hydrographic section along the WOCE AR7W (red line on the inset) with mean temperature shading and density $\sigma = \rho - 1000$ (in kg/m^3) (denoted by white contour lines with contour interval 0.05 kg/m^3). Positive (negative) velocity contours are shown in black solid (dashed) lines (contour interval is 10 cm/s). The red vertical lines highlight the limits of the boundary current for the barotropic streamfunction (black dashed line on the inset). The color shading on the inset represents the mean surface temperature. (b) Late spring (May-June) mean potential vorticity (PV) along WOCE AR7W. Red lines denote the $4 \cdot 10^{-12}$ $(m\ s)^{-1}$ contour of the PV. White dashed lines are the isopycnals bounding the convected water. All values are averaged over the years 16-20.

CHAPTER 4

DENSE WATER PATHWAYS

This chapter deals with the passive tracer analysis performed in this study. Qualitative insight is given in boundary current-induced changes in the export pathways and residence times of both dense convective waters that were formed in the interior and lighter convective waters that were formed in the boundary current itself.

4.1. Initialization of passive tracer in the convection area

This study makes use of a passive tracer analysis to investigate the pathways of water masses from their formation region (e.g. in the interior or the boundary current) to the exit of the Labrador Sea via the boundary current (see also Figure 1.3). The first tracer is initialized in the core of the convection area, outside the influence of the boundary current. The tracer is released with values of one at the start of year 16 (after the system has equilibrated) and is monitored for a period of five years. It has a cylindrical shape with a diameter of 375 km and extents from the surface to a depth of 1575 m. This corresponds to an approximate depth of the winter mixed layer for each simulation (see Section 3.3). Figure 4.1 visualises the initial release of the tracer in the convection area for REF.

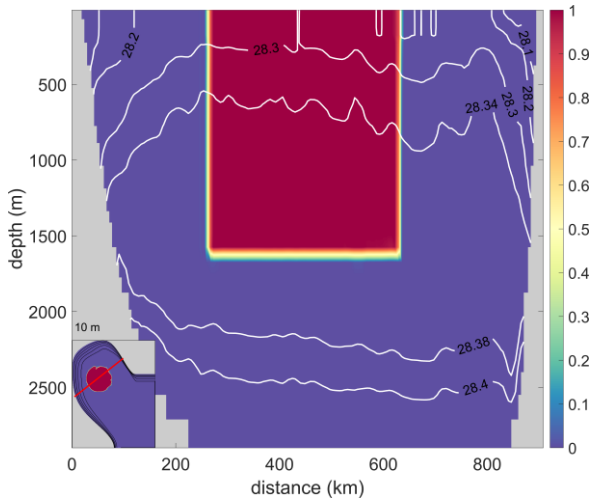

Figure 4.1 Cross-section of the concentration of the passive tracer at the start of year 16 for REF. Density $\sigma = \rho - 1000$ (in kg/m^3) is denoted by white contour lines. The inset shows a snapshot of the tracer close to the surface. Red line highlights the selected section. Black lines denote the isobaths with intervals of 500 m.

Chapter 3 already showed the complexity of the dynamics due to relatively small changes in the boundary current strength. In order to compare the pathways, it is decided to not match the location of the passive tracer with the core of the convection area for each scenario (see maximum MLD, Figure 3.3). This study aims to perform a monothetic analysis (i.e. testing of factors, one-at-a-time instead of multiple factors simultaneously), in this case the effect of export pathways of convective waters due to changes in the boundary current. To this end, the shape and release location of the passive tracer are the same for WEAK/STRONG.

4.2. Pathways of dense convective waters formed in the interior

Figure 4.2 shows snapshots of the tracer concentration at different depth layers (e.g. $10\ m, 575\ m, 962.5\ m, 1337.5\ m, 1575\ m,$ and $1987.5\ m$), one year after the release [4]. Figure 4.3a shows a cross-section along the convection area and the boundary current (close-up at the topographic narrowing in Figure 4.3b). Notably, the tracer is brought to deeper layers by the process of convection: the concentration peaks between depths of approximately $800 - 1800\ m$, while the tracer was initially released to a maximum depth of $1575\ m$. From deeper layers it is steered eastward by the strongly sheared velocity field, which is associated with the high eddy activity. The eddies, originating from barotropic instabilities at the topographic narrowing, steer these convected waters into the boundary current at the eastern side of the basin. Once entrained, they are exported out of the Labrador Sea following the boundary current. In the idealized model studies of Brüggemann and Katsman (2019), and Georgiou et al. (2019), this route is referred to as the indirect export route.

The snapshots of Figure 4.2 give a good impression of this export mechanism. In particular, at deeper layers (e.g. $1337.5\ m$ or $1575\ m$), a quasi-geostrophic turbulent picture emerges, showing the passive tracer kept by a swirling motion. The eddy-induced shear flow directs the tracer into the boundary current in the north-east of the basin. From the north-east towards the exit, a tail-shaped concentration in the boundary current is evident for this indirect export pathway. Figures 3.2a and 4.3a-b show that the isopycnals are strongly tilted downward in the direction of the boundary current as a result of the buoyant waters that encircle the basin. The associated density gradients reduce in downstream direction due to the barotropization of the boundary current (see Section 3.1), and consequently isopycnals rise. Therefore, it might be easier for the densest convective waters to enter the boundary current at the western side of the basin. Though, one major constraint is that this entrainment can only take place where the density and depth of the convective water masses match the local water mass properties of the boundary current (Georgiou, 2021). Therefore, an eddy-induced shear flow is needed to steer these waters downward into the boundary current. According to Figure 3.3, we found the most intense eddy activity (highest EKE) is at the topographic narrowing. To this end, enhanced downwelling is concentrated close to this West-Greenland coast which goes along with a strong vertical velocity component (Brüggemann & Katsman, 2019; Georgiou, et al., 2019). At first sight, this seems a rather inefficient export route for convective waters formed in the interior, but the preconditions for entrainment into the boundary current explain the export route (e.g. match in density and depth; eddy-induced shear flow).

In Chapter 3 we described that due to weakening/strengthening of the boundary current, a chain of reactions led to significant changes in the dynamics of the Labrador Sea (e.g. the overturning strength; the eddy kinetic energy (EKE); the depth of the mixed layer (MLD); the density of convective waters). Therefore, we expect changes in the export routes of convective waters. The release of a passive tracer enables us to qualitatively assess the effect on those export pathways and compare the differences among each scenario. Considering the distribution of the tracer in depth-space (Figure 4.2), we observe a higher (lower) concentration at shallower depth ($< 1000\ m$) for STRONG (WEAK) compared to REF. The opposite holds for the deepest layers ($> 2000\ m$): lower (higher) concentrations for STRONG (WEAK) compared to REF (see also Figure 4.3a). Despite the changes in depth, most of the tracer is confined to the scenario-specific isopycnal limits of convective waters. These limits are given in Table 3.1 and highlighted in Figure 4.3a-b. As expected, at the west coast of Greenland the tracer is laterally transported towards the boundary current along isopycnals in all three scenarios (Figure 4.3b).

[4] Supplementary material (animation of the first year after release) is accessible via this link.

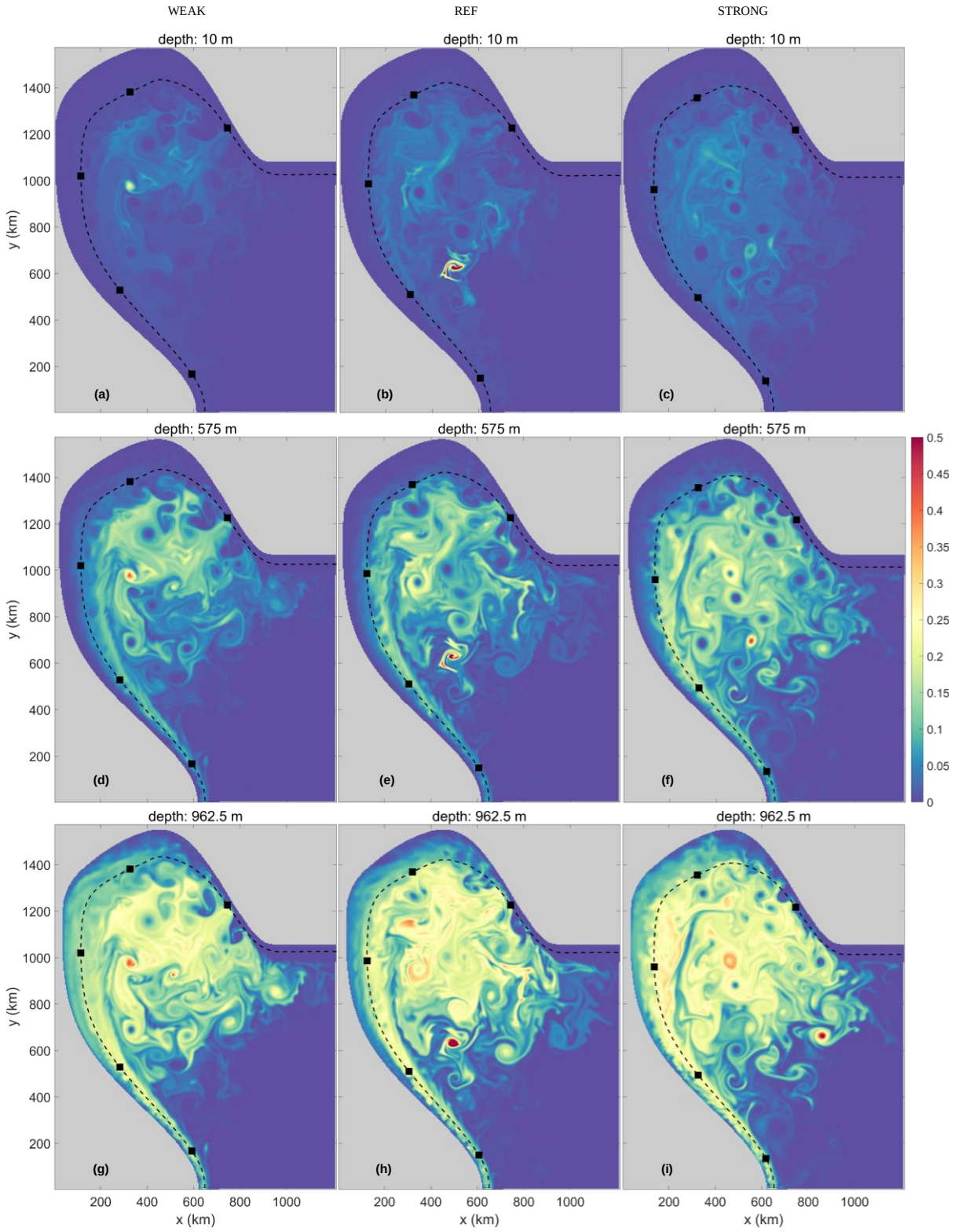

Figure 4.2 – part 1. Snapshots of passive tracer concentration at the end of year 16 for (left column) WEAK, (middle column) REF, (right column) STRONG and at depths (top row) 10 m, (middle row) 575 m, (bottom row) 962.5 m. Black dashed line indicates the barotropic streamfunction for contour line 17 Sv (WEAK), 18 Sv (REF), 19 Sv (STRONG). Black markers are placed on an interval of 500 km from inflow at the southern tip of Greenland.

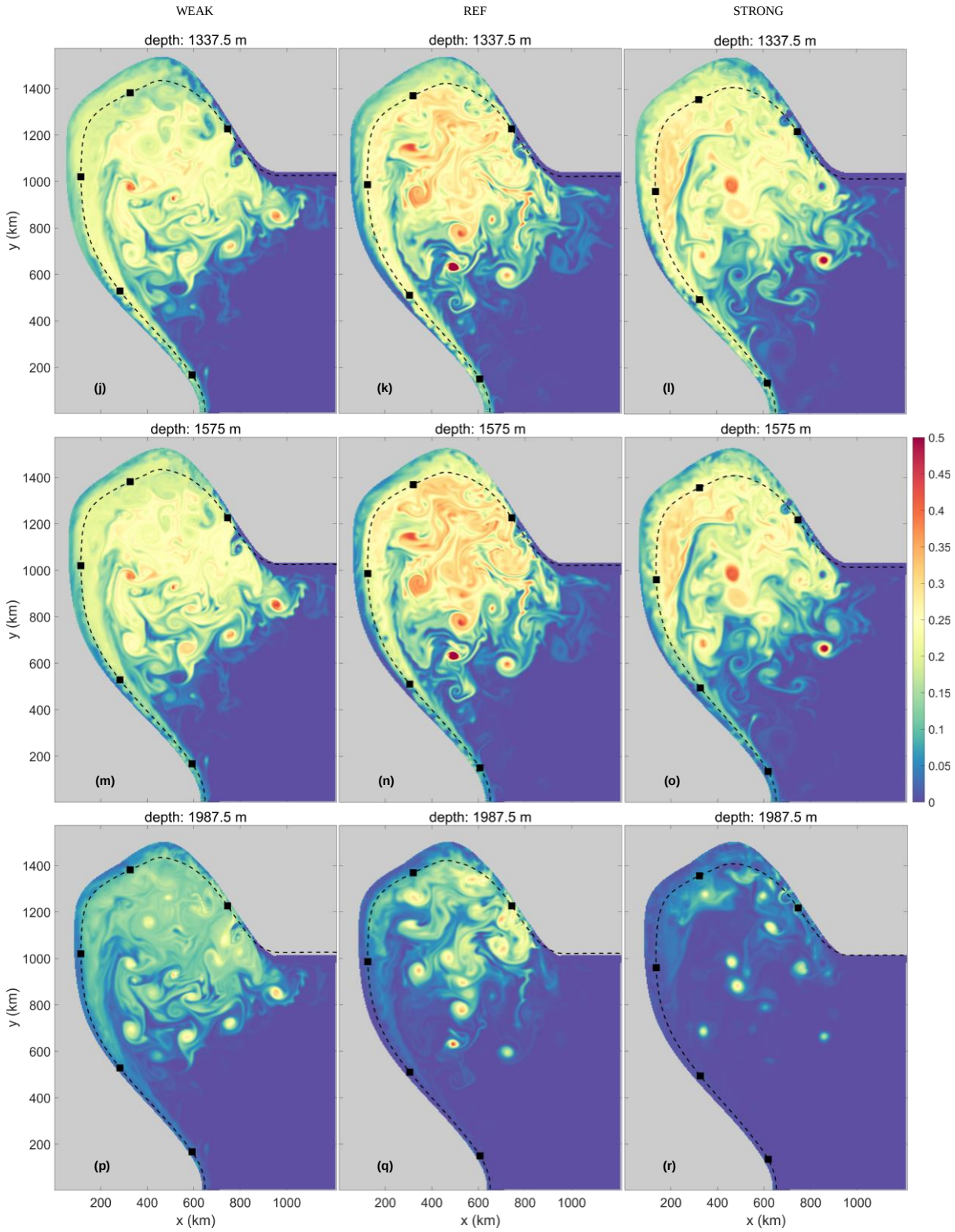

Figure 4.2 – part 2. As Figure 4.2 – part 1, but at depths (top row) 1337.5 m, (middle row) 1575 m, (bottom row) 1987.5 m.

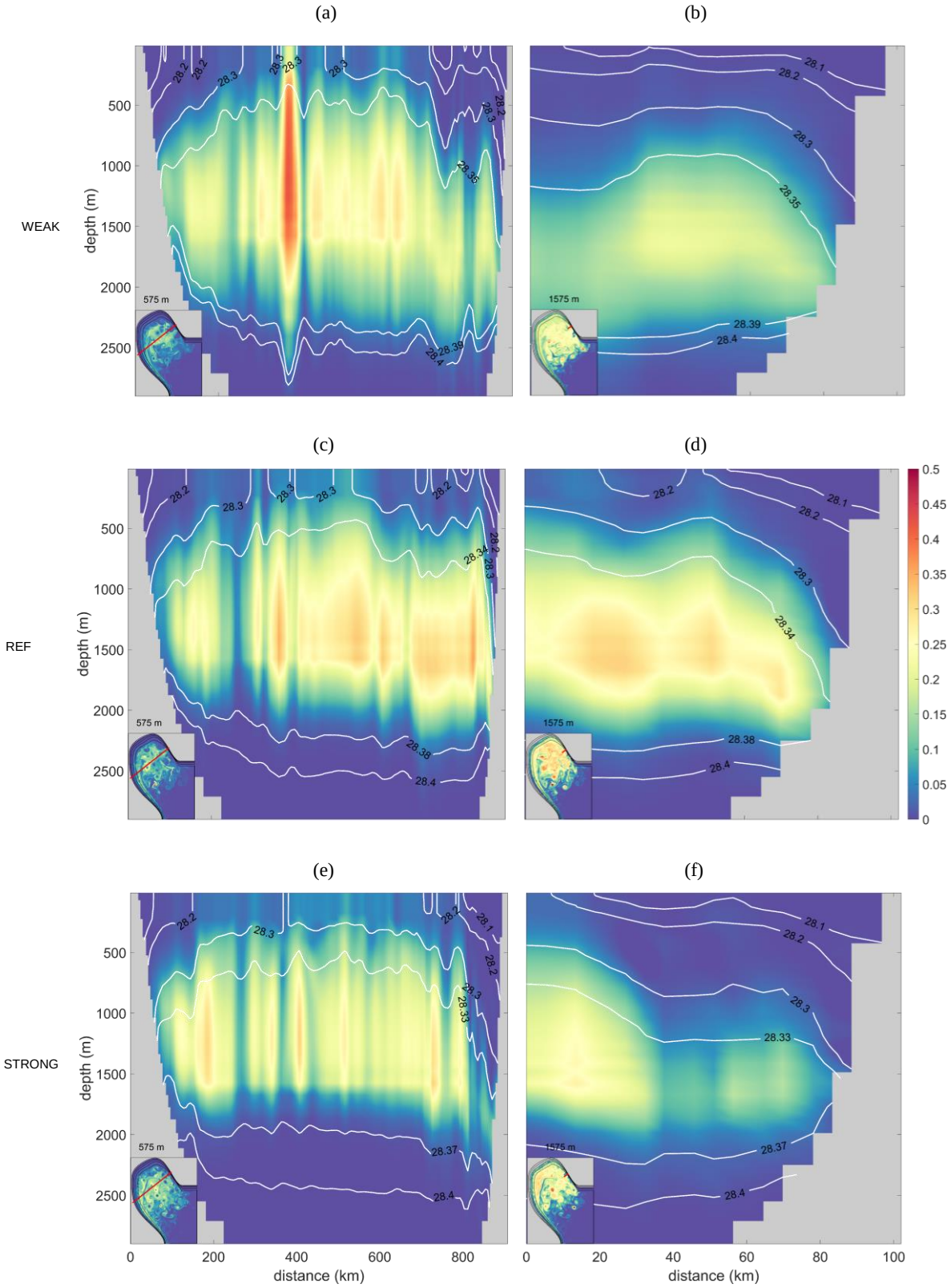

Figure 4.3 Snapshots of passive tracer concentration at the end of year 16. (left column) section over the basin's width, and (right column) a close-up of the West-Greenland coast. Density $\sigma = \rho - 1000$ (in kg/m^3) is denoted by white contour lines (in particular the isopycnals are highlighted that bound the convected waters for each specific simulation (see Table 3.1). The insets show snapshots of the concentrations at specific depths (similar to Figure 4.2). Red lines highlight the sections. Black lines denote isobaths with intervals of $500\ m$.

Figure 4.4 shows the concentration of the tracer along the barotropic streamfunction averaged over the first year from it release. The barotropic streamfunction (defined in Section 3.1) separates the boundary current from the interior, and is unfolded in Figure 4.4 from the inflow location towards the exit. Notably, the tracer crosses the barotropic streamfunction mostly between $500 - 1000\ km$ from inflow. It consecutively enters the boundary current before being exported out of the basin. In STRONG (Figure 4.4c), the tracer is more spread along the barotropic streamfunction, suggesting that some tracer enters the boundary current farther downstream.

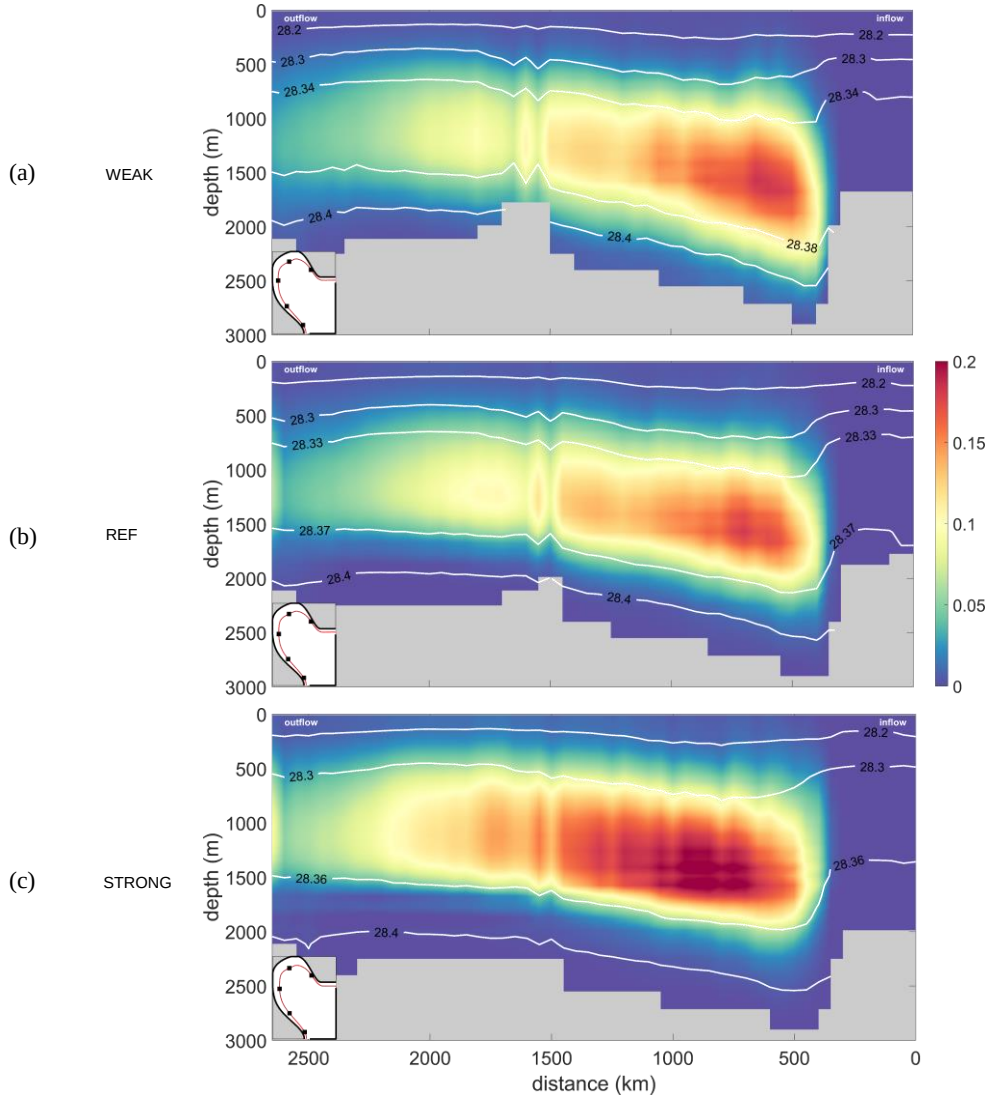

Figure 4.4 Time-averaged (over year 16) passive tracer concentration along the barotropic streamfunction for contour line 17 Sv (WEAK, a), 18 Sv (REF, b), 19 Sv (STRONG, c). Black markers are placed on an interval of $500\ km$ from inflow at the southern tip of Greenland. Distance represents the unfolded barotropic streamfunction. Density $\sigma = \rho - 1000$ (in kg/m^3) is denoted by white contour lines. In particular, the approximate isopycnals that bound most of the tracer are highlighted.

Though, the passive tracer analysis cannot follow the tracer. Consequently, no distinction can be made between tracer that enters the boundary current and tracer that is advected via the boundary current (but has entrained more upstream). In other words, you cannot observe how much tracer is exchanged between the interior and boundary current at a particular location. Nevertheless, Figure 4.4 shows that

most tracer (re)-entrains the boundary current along isopycnals at shallower depth for STRONG compared to REF and WEAK. Averaged over the first year, the concentration is most intense for STRONG (Figure 4.4c). The differences in intensity between WEAK (Figure 4.4a) and REF (Figure 4.4b) are a bit counterintuitive: it seems that an equal amount of tracer enters the boundary current or even more in case of WEAK.

A more quantitative way of analysing the export of tracer under varying boundary conditions is presented in Figure 4.5. It shows the timeseries of the total tracer concentration within the boundary current (i.e. $C_{tot}(t)|_{B_i(x,y,z)} = \iiint c(x,y,z,t)\mathrm{d}x\mathrm{d}y\mathrm{d}z$). The triple integral denotes the laterally and vertically integrated tracer concentration from coast to the scenario-specific barotropic streamfunction. t is the time over the last five years of the model simulation. The boundary current is divided into two regions (i): 1. upstream region at the West-Greenland side (eastern side of the basin); 2. downstream region at the Labrador side (western side of the basin). The boundary current is highlighted in yellow on the inset in Figure 4.5, including the line that separates the two regions. The rest of the basin is masked.

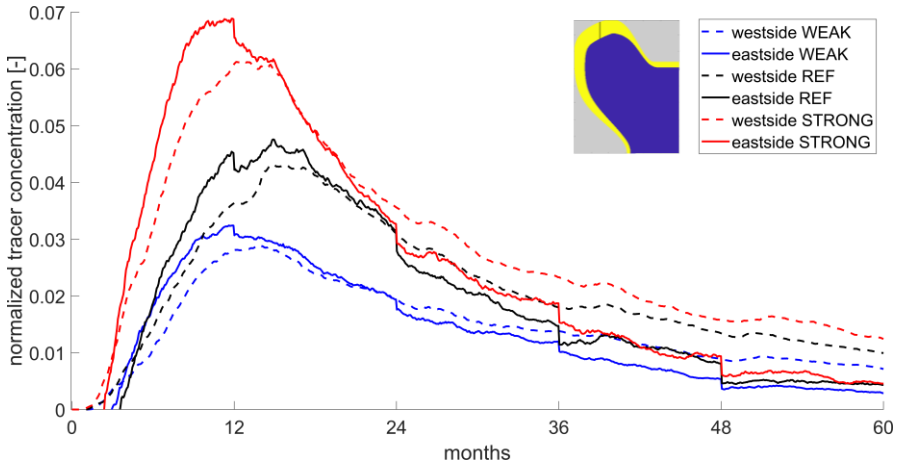

Figure 4.5 Five-year timeseries of total amount of normalized tracer concentrations in the boundary current. The boundary current (yellow mask on the inset) is split into two sections: 1. upstream region at the West-Greenland side (eastern side of the basin, solid lines); 2. downstream region at the Labrador side (western side of the basin, dashed lines). [5]

For all three scenarios, the concentration first peaks at the eastside (solid line) and then at the westside (dashed line). One could compare the peak in concentration with a river's flood wave, which arrives at a later instant downstream and has a diffusive character (e.g. the concentration spreads). This would suggest that for all scenarios the tracer first arrives at the West-Greenland side and then is advected in downstream direction towards the exit of the Labrador Sea.

The timescale of the indirect path (from the interior towards the west coast of Greenland) is shorter for STRONG than for REF and WEAK. Possible explanation for the early entrainment at the west coast in case of strengthened boundary current is as follows: convected waters in STRONG (WEAK) can enter the boundary current more (less) easily due to higher (lower) eddy-induced shear flow that steer these waters into the boundary current. With a strengthened (weakened) boundary current, more (less) energetic eddies detach at the topographic narrowing and squeeze the convective waters along

[5] The apparent jumps at the start of each model year only appear at the eastside, suggesting that the tracer is not properly conserved in this calculation method. Therefore, care should be taken interpreting this figure, and it is only used to show the differences in timescales among the scenarios.

isopycnals into the boundary current. This effect can be enhanced by the following: the convected waters in STRONG (WEAK) are located higher (lower) in the water column (Figure 4.3a-c-e). Because the strength of eddy-induced shear flow decreases with increasing depth (Georgiou, et al., 2019), shallower waters (i.e. the lighter convected waters) experience the steering most effectively.

However, the response to a change in the boundary current strength is not fully symmetric: Figure 4.5 tells us that dense waters arrive earlier at the West-Greenland side in WEAK compared to REF. Though, in terms of volume, REF quickly outpaces. Another notion is that some tracer first arrives in the downstream end of the boundary current at the Labrador side (red/black/blue dashed lines, Figure 4.5). As this occurs directly after release of the passive tracer, this tracer is most likely influenced by the presence of the boundary current. This will be outlined in the next section.

4.3. Isopycnal fingerprints of dense convective waters formed in the interior

Next, we aim in identifying the density of water masses for specific export routes, and the location where they entrain into the boundary current. To do so, we calculate the total tracer concentration that is found within certain density bins ($\mathrm{d}\rho = 0.005\ kg/m^3$) integrated over different cross-sections within the boundary current (i.e. $\mathrm{C}_\rho(\rho,t) = \int_{P(x_1,y_1)}^{P(x_2,y_2)} \int_{z_1(\rho)}^{z_2(\rho+\Delta\rho)} c(t)\,\mathrm{d}P\mathrm{d}z$). Here, $\mathrm{P}(x,y)$ is a specified plane section extending from the coast towards the scenario-specific barotropic streamfunction, and from surface to the sea floor at $3000\ m$. The first cross-section (Figure 4.6) is chosen after the narrowing, approximately at the split of the boundary current regions in Figure 4.5. The second cross-section (Figure 4.7) is chosen in the west, close to the exit of the marginal sea.

In all three scenarios we see that there is a peak of the tracer concentration between the isopycnals that define the convected waters in each scenario (defined in Section 3.4, dashed lines in Figures 4.6, 4.7, top panel). These isopycnal limits correspond to the density space at which the tracer entered the boundary current (Figure 4.4). The relatively high concentration peak at lower densities in Figure 4.6 (i.e. above the dashed line) shows that the entrainment criteria is less (more) strict for STRONG (WEAK) than for REF. It suggests that in STRONG also lighter convected waters can entrain. This is possibly due to the increased strength of the eddy-induced shear flow in combination with the shallower depth at which the lighter convective waters are located in STRONG. Eddies effectively steer those lighter waters towards the boundary current. In WEAK, the lighter product is located deeper in the water column, where the influence of eddies is less. Therefore, these lighter waters need to become denser before they can enter the boundary current.

In all three scenarios, the first signal is picked up after $\pm$ 3 months (as can be seen from Figures 4.6 and 4.7). More specifically, the time it takes to arrive at the section slightly decreases (increases) with increasing (decreasing) boundary current strength. This timescale can be further analysed based on the depth at which the water masses were located before (and while) undergoing a transformation at the start of year 16. Based on density, the initialization of the passive tracer was split into two: 1. tracer in upper layers $\sigma = \rho - 1000 < 28.3\ kg/m^3$ (middle panel, Figure 4.6, 4.7); 2. tracer in deeper layers $\sigma = \rho - 1000 \geq 28.3\ kg/m^3$ (bottom panel, Figure 4.6, 4.7). Tracer 2 is still confined by a maximum release depth of $1575\ m$ as described in Section 4.1. The top panel of Figures 4.6 and 4.7 shows the combined tracer (tracer 1 + 2). While the top panel of Figures 4.6 and 4.7 are tracers with no differences in volume release between the scenarios, the split causes to change the ratios as it is based on the density structure per scenario. Consequently, STRONG (Figures 4.6f, 4.7f) contains a higher concentration of tracer 1 than REF (Figures 4.6e, 4.7e) and WEAK (Figures 4.6d, 4.7d). The opposite holds for tracer 2: WEAK (Figures 4.6g, 4.7g) contains a higher concentration of tracer 2 than REF (Figures 4.6h, 4.7h) and STRONG (Figures 4.6i, 4.7i). To this end, it is not valid to compare the scenarios among them for

tracer 1 and 2 (only the top panel has the same amount of concentration, tracer 1 + 2). Though, the qualitative pattern for its timing and location in density space can be compared, and reveal unique fingerprints for dense waters that originate from the interior of the basin.

Even the waters that started in upper layers (tracer 1, middle panel, Figures 4.6, 4.7) quickly sink to deeper layers and are not significantly delayed from waters that already were located at depth (tracer 2, bottom panel, Figures 4.6, 4.7). Therefore, it is possible to observe dense water masses that underwent a significant water mass transformation soon after wintertime convection, that make their way out of the Labrador Sea. For both upper and deeper layer waters, the signal is most intense in the first two years, but extends multiple years i.e. after five years tracer is still being exported within its defined isopycnal limits.

This has possible implications for measurements of water mass properties of water being exported out of the Labrador Sea. The lighter (denser) product due to a strengthening (weakening) of the boundary current in one year could already be measured within the first year at the exit location of the basin. Though, the exported convected waters are a mixture of multiyear convected waters. Consequently, the densities of water masses that exit the Labrador Sea in one year show signs of variations in the boundary current of that specific year (despite taking the indirect route). However, the density of the transported water is also affected by the water masses formed in previous years. In other words, there is 'memory' in the Labrador Sea in which the density of the LSW in one year is related to among variations in boundary current strength of previous years (i.e. autoregressive effects).

The observational study of Rykova et al. (2015) already suggested that the LSW properties are controlled by changes in the boundary current on interannual timescales, and by changes in surface fluxes (Rykova, et al., 2015; Georgiou, et al., 2019). Their results of the surface circulation derived from satellite altimetry data suggest that the increase in eddy activity is due to an increase in the baroclinicity of the boundary current, with implications for lateral heat fluxes tied to the eddy production (Rykova, et al., 2015).

Once it passes the section at the western side of the Labrador Sea (Figure 4.7) the tracer is diffused and delayed. In STRONG (Figure 4.7c) a weak signal is present at start. As it is not present at the West-Greenland coast (Figure 4.6c), it must have entered the boundary current at the westside of the interior. The split-up tells that it is tracer 2 that takes this direct route (Figure 4.7i). A possible explanation is that some deep water is entrained by the fast-flowing current in STRONG.

All other plane sections are given in Appendix B.1. Figures B.2, B.3, and B.4 give a good impression of the water mass properties and the location where they entrain into the boundary current. The densest waters enter more upstream at the topographic narrowing than the lighter waters (e.g. compare Figure B.3 with Figure B.4). Possibly, due to barotropization of the boundary current (Section 3.1) the isopycnals rise, therewith opening the pathway for convective waters at shallower depth. That pathway is effective due to the presence of eddies that steer these waters into the boundary current. At other locations along the boundary current, the absence of energetic IRs or BCEs result in convective waters not being able to advect along isopycnals into the boundary current.

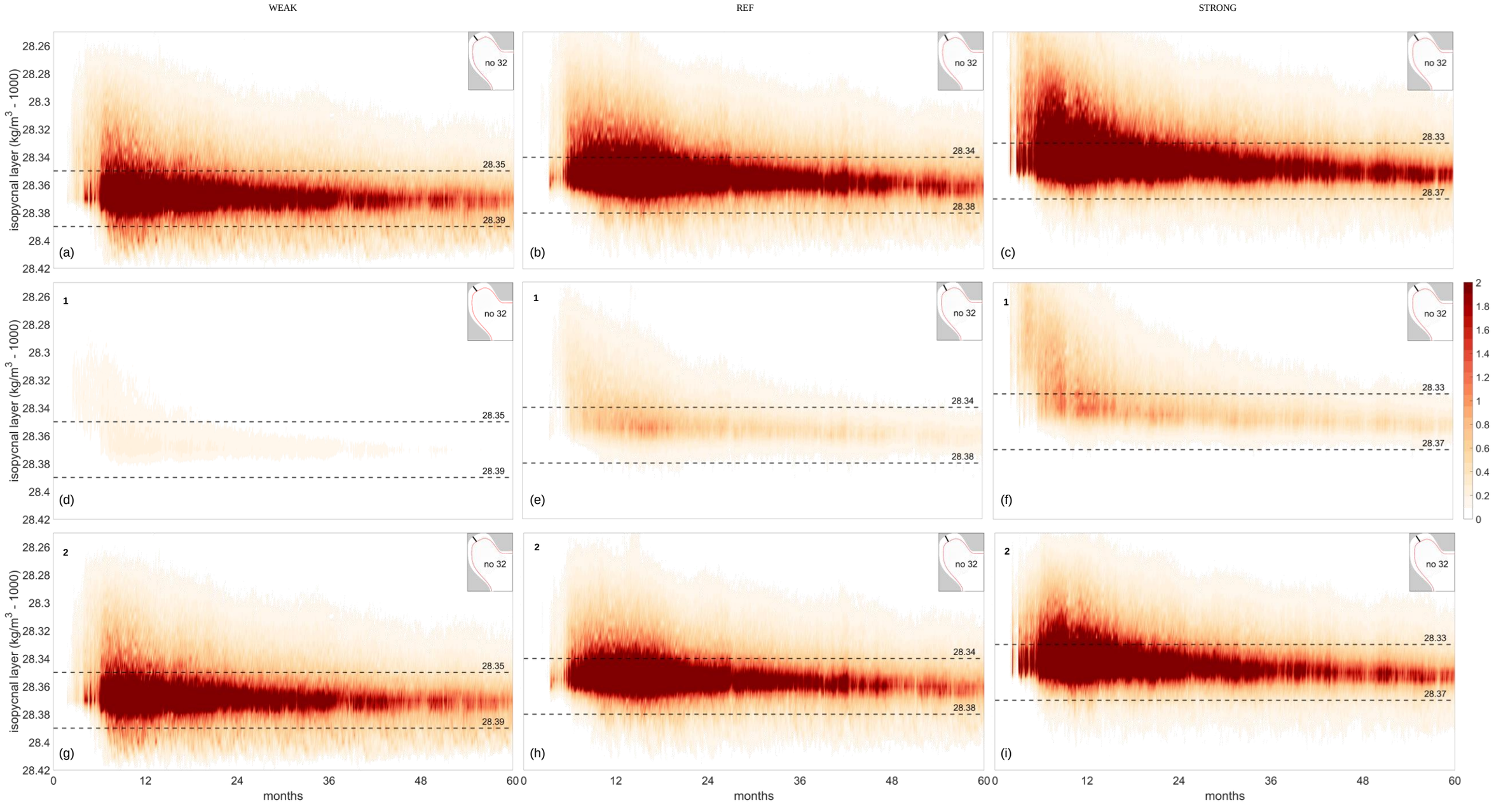

Figure 4.6 Amount of passive tracer transported by the boundary current within different isopycnal layers over five years after release for WEAK (left column), REF (middle column) and STRONG (right column). The signal is split up into tracer that was initially released in surface waters of the interior $\sigma = \rho - 1000 < 28.3\ kg/m^3$ (tracer 1) and released in deeper waters $\sigma = \rho - 1000 \geq 28.3\ kg/m^3$ (tracer 2). The boundary current is defined by the barotropic streamfunction for contour line 17 Sv (WEAK), 18 Sv (REF), 19 Sv (STRONG). The location of the section is highlighted on the inset. Black dashed lines denote limits of convective waters per scenario.

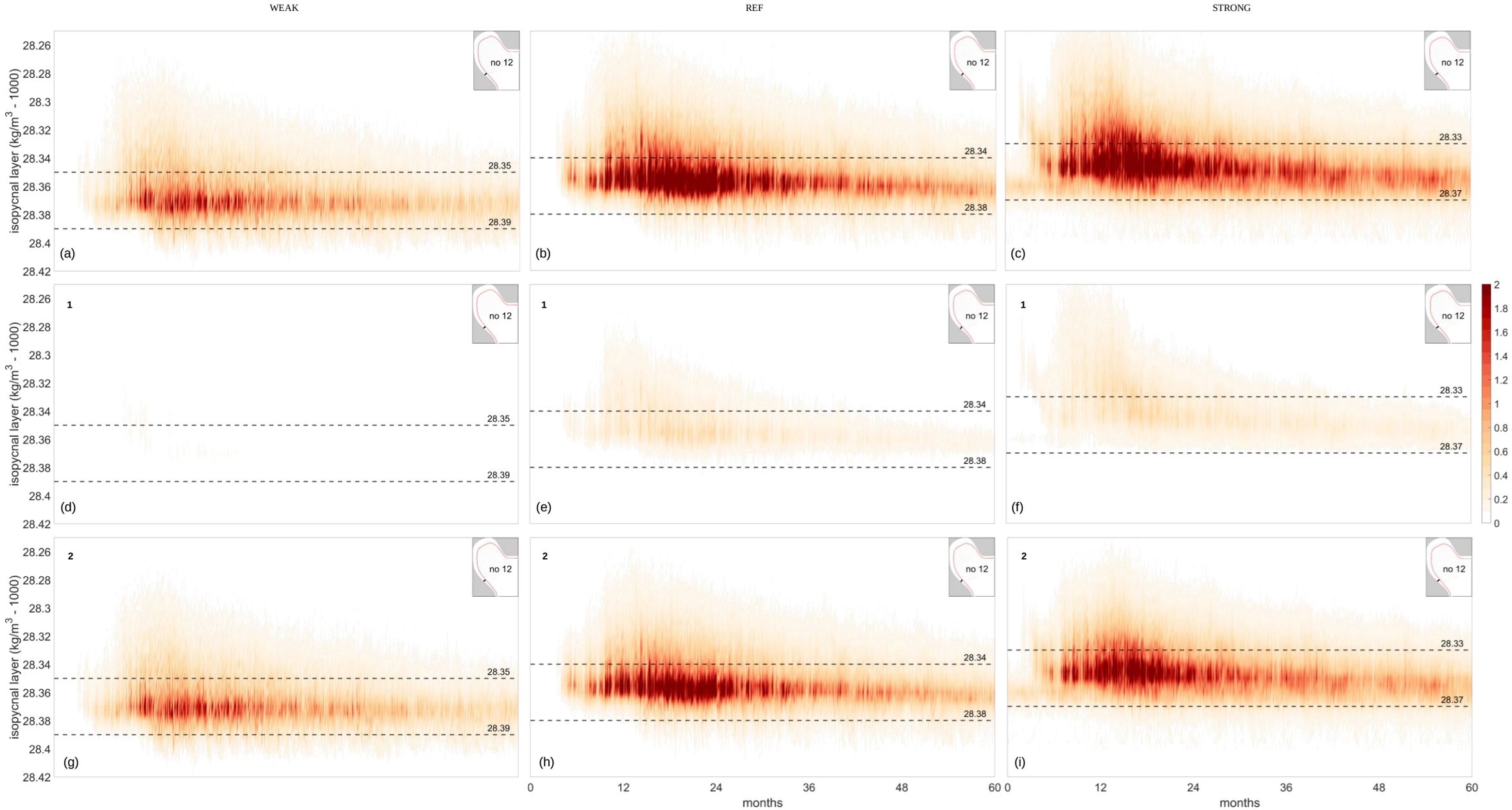

Figure 4.7 Same as Figure 4.6, but for a different cross-section in the boundary current (more downstream)

4.4. Initialization of passive tracer in the boundary current

In the previous sections attention was paid to the overturning mechanism involving water mass transformation by deep convection in the interior. Eddies are responsible for the transport of these waters into the boundary current prior to be exported out of the Labrador Sea. A second overturning mechanism is present in the boundary current itself. The boundary current loses heat via lateral advection of heat by the eddies and via atmospheric cooling. This allows for the process of convection to also occur within the boundary current itself. According to Brüggemann and Katsman (2019), this mechanism is very time-efficient as these waters are confined to the fast-flowing boundary current (Brüggemann & Katsman, 2019). The product of convection in the boundary current is lighter than water masses formed in the interior because the boundary current is still stratified once it exits the basin. To verify this mechanism for the idealized Labrador Sea model, a passive tracer was initialized at the inflow from surface to bottom.

4.5 Pathways of light convective waters formed in the boundary current

Similar to the analysis performed in Section 4.2, the snapshots of the passive tracer concentration are shown in Figure 4.8 at different depth layers (e.g. $10\ m$, $575\ m$, and $1575\ m$), 160 days after the release (e.g. around mid-May) [6]. As expected, the tracer is quickly exported out of the basin via the boundary current in all three scenarios. At deeper layers (say $1575\ m$) there is hardly any tracer in the boundary current region. This suggests that the product of convection in the boundary current is exported in upper layers with lower densities, compared to water masses that are convected in the interior. In all scenarios, some tracer is brought into the interior by eddies at the west coast of Greenland. These buoyant waters are expected to undergo deep convection prior to exiting the interior. The associated timescales of these water masses are longer compared to water masses that undergo convection within the boundary current itself. The higher concentration at the inflow (Figures 4.8d-i) is due to the initialisation of tracer in deeper layers, where velocities are almost zero (Figure 3.2a).

The timeseries in Figure 4.9 show the total amount of normalized tracer concentration for the tracer that was released at the inflow of the boundary current. Because the high concentrations at the inflow in deeper layers distort the picture on export timescales of these waters (see supplementary material and Figures 4.8d-i), we only consider the passive tracer that is located in a high velocity zone at the start of year 16. More specifically, the tracer that is initialized in the boundary current for $\boldsymbol{u} \geq |0.1|\ m/s$ (Figure 2.2b). Now, Figure 4.9 reveals the export timescales of convected waters formed within the boundary current. For all three scenarios, approximately 60% of the lighter convective waters have left the Labrador Sea after one year, and after five years 80-85%. The export timescales are close together for all simulations and no proportionality can be derived between the boundary current strength and the export timescales of light convective waters formed within the boundary current. This suggests that slight changes in the boundary current strength have negligible effect on the export timescales of these lighter convective waters.

[6] Supplementary material (animation of the first year after release) is accessible via this link.

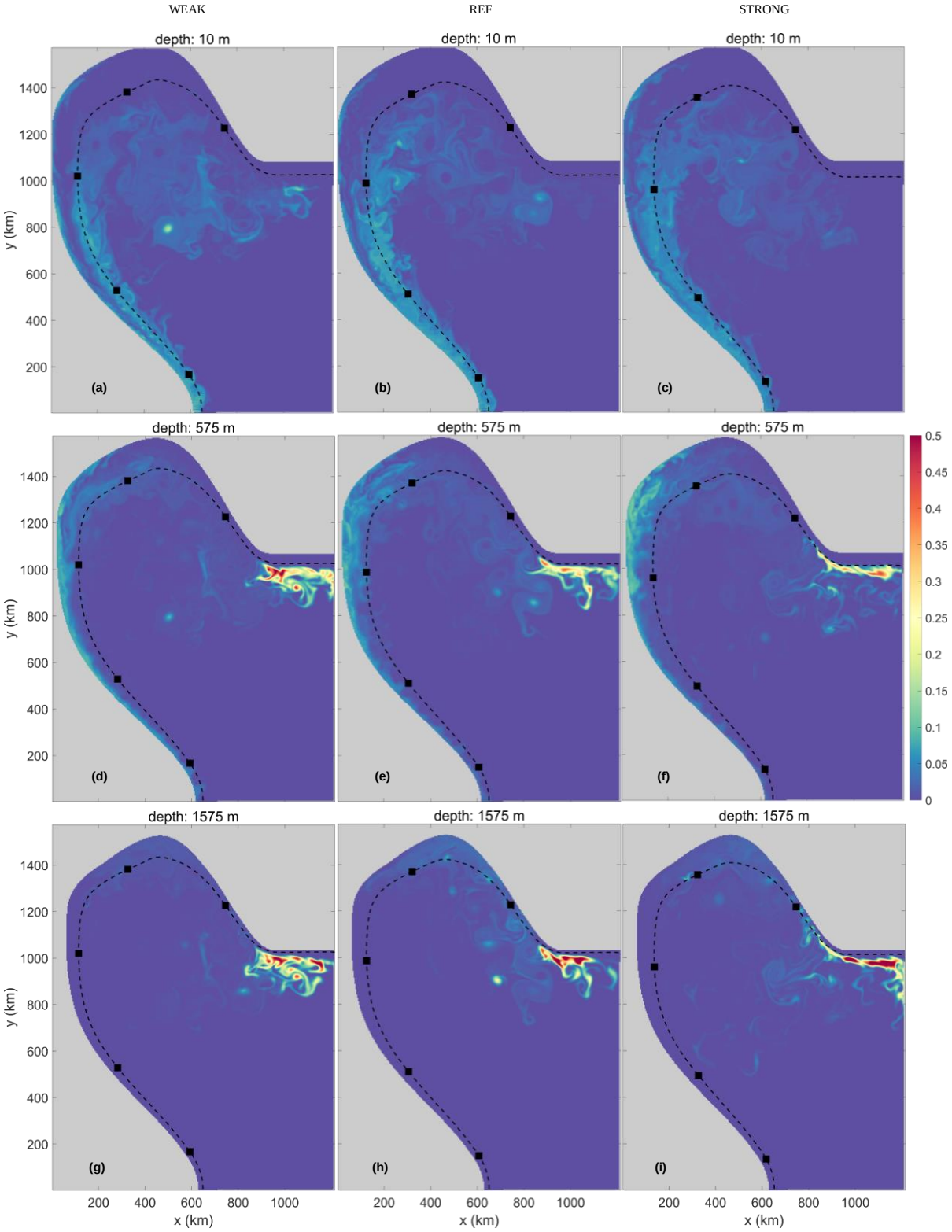

Figure 4.8 Snapshots of passive tracer concentration 160 days after the release for (left column) WEAK, (middle column) REF, (right column) STRONG and at depths (top row) 10 m, (middle row) 575 m, (bottom row) 1575 m. Black dashed line indicate the barotropic streamfunction for contour line 17 Sv (WEAK), 18 Sv (REF), 19 Sv (STRONG). Black markers are placed on an interval of 500 km from inflow at the southern tip of Greenland.

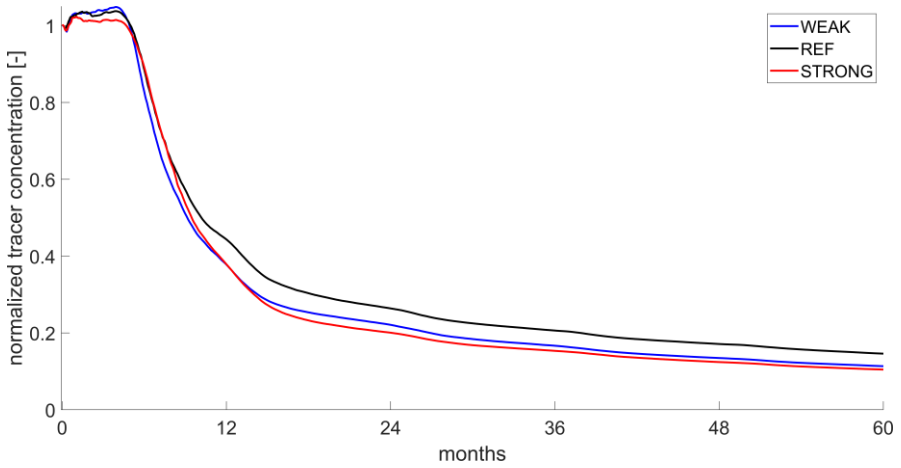

Figure 4.9 Five-year timeseries of basin-total amount of normalized tracer concentration that was initialized in the boundary current for $\boldsymbol{u} \geq |0.1|\ m/s$. Note that the concentration is normalized, meaning that the volumes are scaled.

4.6. Isopycnal fingerprints of light convective waters formed in the boundary current

Similar to the integration method applied in Section 4.3 for the convective waters formed in the interior, along-isopycnal integration led to the signals in density space for the passive tracer released in the boundary current. The isopycnal fingerprints are shown in Figure 4.10 for all three scenarios at three different cross-section along the boundary current. For all cases, the signal is picked up much higher up in the water column at the exit location, indicating a lighter export product. In addition, the surface waters in the boundary current transform into denser water masses as the boundary current cools along the perimeter due to atmospheric cooling, and due to lateral eddy heat fluxes (Brüggemann & Katsman, 2019). This becomes clear from Figure 4.10 when following the tracer in downstream direction: convection occurs within the boundary current itself for these upper layer waters. Note, that the high concentration for $\sigma = \rho - 1000 \geq 28.3\ kg/m^3$ is due to the initialization of the passive tracer at inflow in deeper layers (Figures 4.8g-i).

The isopycnal fingerprints confirm the short timescale of these lighter convective waters. Within one year, most tracer has left the basin. Though, no proportionality can be derived between the boundary current strength and the export timescales. Variations in the boundary current strength yield less pronounced differences in pathways and residence times for the lighter convected waters formed within the boundary current, compared to the denser convected waters formed in the interior.

Going back to Figure 4.10, after one year the tracer is confined to the isopycnal bounds of dense convective waters. Possibly, this tracer was either brought into the interior by eddies, and underwent diapycnal mixing in the interior, before it entrained at deeper layers into the boundary current. This suggests that, already after half a year, dense water masses can be observed that were originally buoyant surface waters when entering the basin. Downwelling of these water masses did not occur in the boundary current itself, but involved a complex interplay between the boundary current-interior and the eddy field. Alternatively, it is tracer from deeper layers at the release location e.g. the deeper waters at the entrance (see Figure 4.8). Based on the tracer analysis only, we cannot draw a solid conclusion from where these dense convected waters originate.

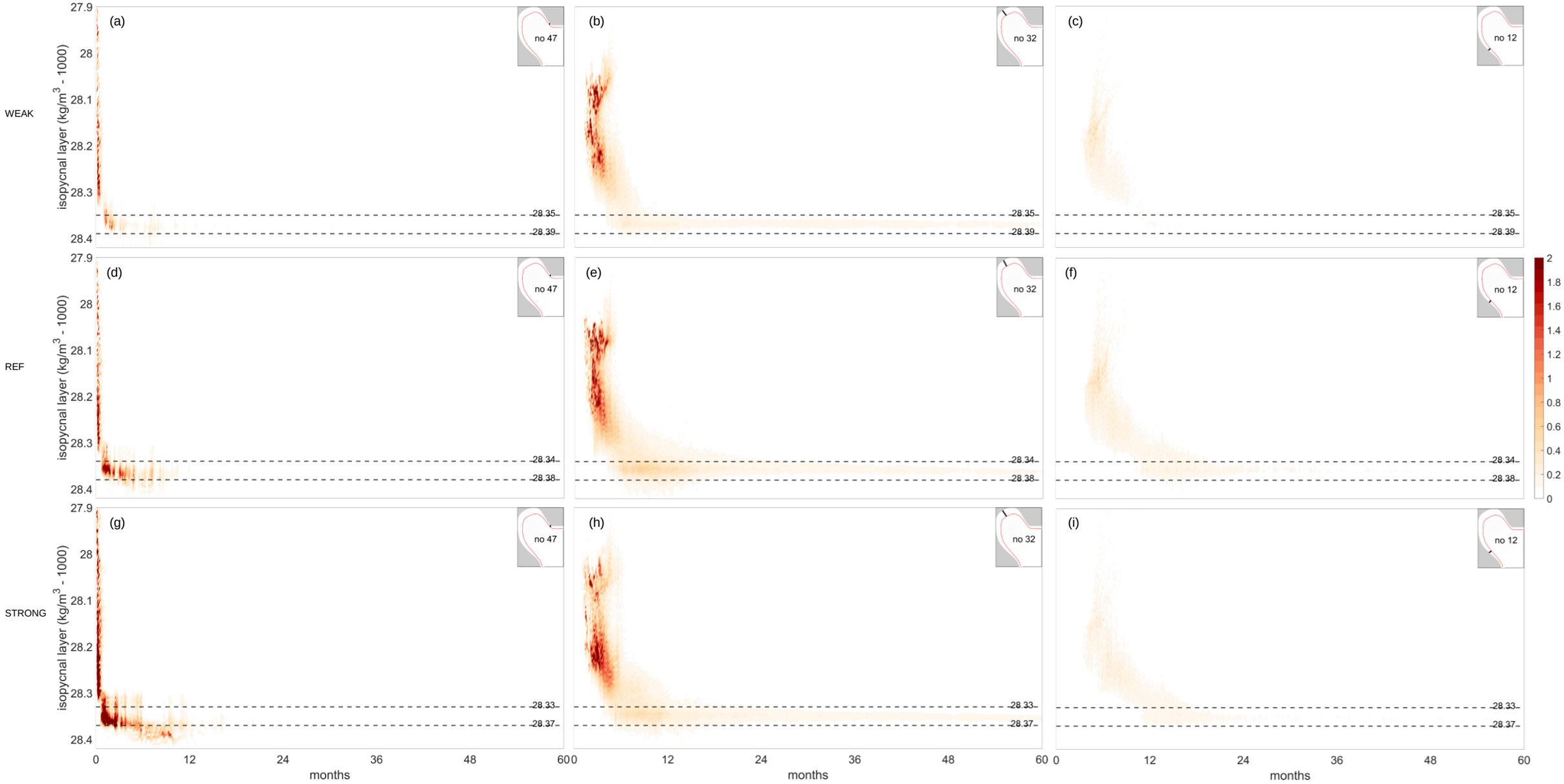

Figure 4.10 Amount of passive tracer transported by the boundary current within different isopycnal layers over five years after release for WEAK (left column), REF (middle column) and STRONG (right column). The passive tracer was initially released in the boundary current at the southern tip of Greenland. The boundary current is defined by the barotropic streamfunction for contour line 17 Sv (WEAK), 18 Sv (REF), 19 Sv (STRONG). The location of the section is highlighted on the inset. Black dashed lines denote limits of dense convective waters formed in the interior per scenario.

CHAPTER 5

CONCLUSION AND DISCUSSION

This chapter summarizes the model results of the preceding chapters and concludes what the effect is of variations in boundary current strength on the product of deep convection, the export pathways and associated timescales of convective waters in the Labrador Sea.

5.1. Summary and conclusions

The overturning in the Labrador Sea and its variability contributes to AMOC variability. According to recent state-of-the-art climate model studies, a substantial weakening of the AMOC is projected over the 21st century. To this end, an increased effort is put in understanding the variability of the LSW production and its export timescales. Among other studies, Georgiou (2021) put the role of the Labrador Sea under renewed debate, and suggest a rather complex interplay between the production of LSW, the boundary current and the eddy field. The existence of multiple export routes and associated residence times highlights that care should be taken when linking AMOC variability to variability in LSW production. The differences in timescales of convective waters to exit the Labrador Sea depends on the pathway and location where these water masses can entrain into the boundary current, after they are formed in the interior of the basin. This transport is constrained by a match between density and depth of the LSW in the interior and the density structure of the boundary current. This led to a complex three-dimensional picture in which the interior-boundary interaction is crucial for the export and properties of the LSW that contributes to the lower limb of the AMOC.

Since entrainment can only take place at locations and depths where both density and depth match the local water mass properties of the boundary current (Georgiou, et al., 2021), this study aims to provide qualitative insight in how variations in the boundary current (both density structure and strength) lead to different export pathways and properties of the LSW. Therewith, we are a step closer in understanding the linkage between Labrador Sea dynamics due to changes in the boundary current strength, and AMOC variability. An idealized eddy-resolving numerical model (reference run, REF, Georgiou et al., 2019) is used to set-up two scenarios in which the density structure of the boundary current differs at the southern tip of Greenland. The variations result in respectively a 5% strengthening (STRONG) and 5% weakening (WEAK) of the boundary current strength, which corresponds well with observed interannual variability of surface velocities (Rykova, et al., 2015). The main question to address is defined as:

What is the effect of variations in boundary current strength on export pathways of convective water masses in the Labrador?

The heat budget analysis in Section 2.3 already revealed that slight changes to the boundary current induce a significant change in locations where mesoscale eddies detach from the boundary current and what their preferred path is when moving towards the interior. For STRONG (WEAK), eddies detach more downstream (upstream) of the topographic narrowing along the West-Greenland coast, and travel farther (less far) into the interior on average (Figure 2.9). The associated eddy heat advection in STRONG (WEAK) is stronger (weaker), implying that eddies carry more (less) buoyant water from the boundary current into the interior. Therefore, the restratification process is more (less) effective in STRONG (WEAK). In addition, the preferred pathways of eddies change the formation location of convective water masses (lateral and depth), and their pathway towards exiting the interior.

Where exactly these water masses exit the interior becomes apparent from the analysis of barotropization (Section 3.1). It showed that the strongest overturning in the Labrador Sea occurs at the topographic narrowing near the West-Greenland coast as already mentioned in earlier studies (e.g. Brüggemann and Katsman, 2019; Georgiou et al., 2019). The overturning strength scales with the boundary current strength (Figure 3.2d). This can be viewed from a perspective of mass conservation: a faster (slower) boundary current is more (less) susceptible to barotropic instabilities along the steepening of the sea-floor bathymetry. Consequently, more (less) energetic mesoscale eddies detach from the boundary current. The buoyant waters spilled at surface need to be compensated at deeper layers. The same eddies are responsible for steering convective waters along isopycnals into the boundary current.

The susceptibility to instabilities is revealed by an increased (decreased) eddy kinetic energy (EKE) near the boundary current with increasing (decreasing) boundary current strength (Figure 3.3). The eddies travel longer (shorter) distances into the interior and carry more (less) buoyant water along with them in STRONG (WEAK). Consequently, the interior restratifies more (less) effectively after wintertime deep convection processes. The analysis of the mixed layer depth (MLD) in Section 3.3 corroborates that the higher eddy activity in STRONG effectively limits deep convection in both horizontal and vertical extent (e.g. shallower MLD and smaller in area, Figure 3.4). In contrast, the MLD in WEAK reaches deeper and covers a larger area. The depth to which deep convection reaches, results in changes in the volumetric weight of the convected water mass product, a lighter (denser) water mass in STRONG (WEAK), respectively (Section 3.4).

Due to the weakening/strengthening of the boundary current, a chain of reactions led to significant changes in the dynamics of the Labrador Sea (e.g. the overturning strength; the eddy kinetic energy (EKE); the depth of the mixed layer (MLD); the density of convective waters). To this end, a passive tracer was released in the convection area of the interior (Figure 4.1) which enables to qualitatively assess the effect on export pathways and compare the differences among each scenario. Figures 4.2-4.4 reveal that the tracer is brought to deeper layers by the process of convection, corresponding to the scenario-specific MLD (Figure 3.3; Figure 4.3a). From deeper layers it is steered eastward by the strongly sheared velocity field, which is associated with the high eddy activity. The eddies steer these convected waters along scenario-specific isopycnals into the boundary current at the West-Greenland coast (Figure 4.3b; Figure 4.4), prior to exiting the basin via the boundary current. This route, from the interior via the west coast of Greenland towards the exit of the basin, is referred to as the indirect export route (Brüggemann & Katsman, 2019; Georgiou, et al., 2019). The most intense entrainment occurs where both the density and depth of the convective water masses match the local water mass properties of the boundary current, and where eddies detach from the boundary current (Figure 4.4).

The timescale of the indirect path is shorter for STRONG than for REF and WEAK (Figure 4.5), possibly because convected waters in STRONG (WEAK) can enter the boundary current more (less) easily due to higher (lower) eddy-induced shear flow that steer these waters into the boundary current. Since the location where mesoscale eddies detach is more downstream (upstream) of the narrowing for STRONG (WEAK), the indirect path from the interior towards the exit is shorter (longer). In addition, the convected waters in STRONG (WEAK) are located higher (lower) in the water column (Figure 4.3a-c-e). Because the strength of eddy-induced shear flow decreases with increasing depth (Georgiou, et al., 2019), shallower waters (i.e. the lighter convected waters) experience the steering most effectively.

In addition to export routes and timescales of convected waters formed in the interior, another passive tracer was released within the boundary current (at inflow) to analyze changes in the export and properties of convected waters formed in the boundary current itself. Results showed (Figures 4.8-4.10) that variations in the boundary current strength yield less pronounced differences in pathways and residence times for the lighter convected waters formed within the boundary current, compared to the

denser convected waters formed in the interior. Accordingly, no proportionality can be derived between the boundary current strength and the export timescales of light convective waters formed within the boundary current. Though, the residence times of these lighter convected waters are short compared to convected waters formed in the interior.

5.2. Discussion

Among observational studies of Rykova et al. (2015) and Pacini et al. (2020) highlighted the importance to investigate the role of the boundary current system in influencing the dynamics in the interior of the Labrador Sea. In particular Rykova et al. (2015) suggested that the LSW properties are controlled by among changes in the boundary current. This study has proven that already slight changes in the boundary current structure (comparable to interannual variability in surface velocity, Rykova et al., 2015) influence the properties of the LSW, the location and depth where they entrain into the boundary current, and the associated export timescales. With help of a passive tracer analysis, isopycnal fingerprints (Figures 4.6-4.7) showed that the convected waters stay bounded to the scenario-specific isopycnals, from entrainment location towards the exit. This means that the lighter (denser) water mass in STRONG (WEAK) can be measured at lower (greater) depths at the exit of the Labrador Sea. The total export of these convected water masses is a mixture of multiyear convected waters: the densities of water masses that exit the Labrador Sea in one year already reflect the variations in the boundary current strength of that specific year, but they also show signs of water masses formed in previous years. Thus, the water mass properties of the LSW (formed in by convection in the interior of the basin) measured in one year are related to among variations in the boundary current strength of previous years (i.e. autoregressive effects). This has implications for linking variability in the LSW production and export to the AMOC variability. Based on density alone, measurements of water masses at the exit do not directly reveal the past-year dynamical state of the Labrador Sea.

Following Georgiou et al. (2019), and based on the above, it is questioned if climate-change scenarios simulated with coarse, non-eddy resolving climate models properly present the physical processes that result in AMOC changes. This study emphasizes that a proper representation of mesoscale eddies in models is necessary for representing the export timescales and water mass properties of the LSW, and their response to changing forcing. Of potential interest is how the production of the LSW and its variability is affected by climate change (Georgiou, et al., 2021). For instance, the increase in freshwater fluxes due to melting of Artic sea-ice and/or the Greenland ice sheet result in a freshening of the boundary current. Van Dam (2018) already used this idealized model of the Labrador Sea to simulate the effects of a freshening of the boundary current, with salinity included in the linear equation of state. According to Van Dam (2018), a freshening lead to increased buoyancy transport and eddy activity in the interior of the Labrador Sea, thereby inhibiting deep convection (e.g. reduced MLD). Similar to STRONG, this yields a lighter export product, potentially slowing down the Atlantic overturning circulation. Van Dam (2018) also revealed that the eddy activity near the boundary current reduces, possibly because the increase in baroclinic instability causes IRs to shed earlier from the boundary current. This might result in long export route as the LSW must entrain farther upstream at the West-Greenland coast. However, the reduced EKE near the boundary current in combination with the shallow located convected waters affect the entrainment volumes and thus export timescales of these waters. It is recommended to simulate these climate-scenarios in combination with a passive tracer analysis to have qualitative insight in the export route, location and depth, and residence timescales under the effect of a freshening.

The simulations performed in recent studies (Van Dam, 2018; Georgiou, et al., 2019; Georgiou, et al., 2020; Woud, 2020) with this idealized eddy-resolving model of the Labrador Sea were forced for a

period of 20 years in order to reach quasi-equilibrium state (Figure 2.7). The aim was to use multiyear diagnostics for the analysis. As mentioned in Section 2.3 this model appeared to be highly sensitive to changes in the density structure of the boundary current, resulting in 'crashing' simulations in early stages. It is of interest to figure out why these models crashed. In addition, diagnostics of early stages can be used to assess the dynamics for more extreme scenarios of changes in the boundary current strength.

It may not be desired to reach quasi-equilibrium in all cases. For instance, it is of interest to see how the Labrador Sea dynamics respond to annual changes in the forcing conditions. As the export of water masses is a mixture of multiyear LSW, the effect of extreme events might be damped by the robustness of the LSW export. To this end, it is recommended to simulate interannual changes to the forcing conditions, in combination with a more statistical approach in which the autoregressive character of the LSW properties are investigated.

Other suggestions for adjustments to this model are the choice of the barotropic streamfunction and the choice of the release location of the passive tracer. The choice for the contour line of the barotropic streamfunction is made to distinguish the boundary current from the interior, but the choice affects the results in the passive tracer analysis. Figure 4.2 reveals that most tracer is advected along the barotropic streamfunction, and the multiple crossing of the tracer with the streamfunction makes it difficult to identify the location where entrainment occurs (Figure 4.4). This qualitative picture of entrainment location becomes more apparent if a more outer-located contour line was chosen.

By changing the release location of the passive tracer to different locations within the interior of the basin, it becomes more clear to what extent the eddies influence the entrainment into the boundary current along West-Greenland coast. In contrast to earlier studies (e.g. Brüggemann and Katsman, 2019; Georgiou et al., 2019, 2020), the direct pathway was not clearly observed. In particular, the preconditions for entraining the boundary current at the Labrador side are not fully understood. In this study, the tracer is located within the convection area of the interior, away from the influence of the boundary current; the tracer first underwent a significant water mass transformation prior to be laterally steered towards the West-Greenland coast. Therefore, it is recommended to release the tracer farther away from the convection zone (e.g. southwest along the Labrador coast, or close to the West-Greenland coast) to reveal their export pathways and water mass properties.

At last, the passive tracer analysis helped to get qualitative insight in the export pathways, export timescales, and water mass properties of the LSW. Though, the tracer cannot be tracked to see where convected water masses exactly enter the boundary current. Only the intensity of the tracer concentration reveals the pattern. This is negatively influenced by the fact that the tracer dilutes with ambient waters. The isopycnal fingerprints fade in downstream direction, while the water masses contract towards the exit. It is recommended to move to Lagrangian particle tracking similar to the study of Georgiou et al. (2020), as it can be used to reveal the possible pathways of convected waters that exit the domain, and the water mass transformation that occurs along these pathways. A huge benefit is that volume transport can be assigned to each particle which is conserved along its trajectory. This enables to quantify the export routes in terms of volume transport and support export routes with statistical analysis.

REFERENCES

Biastoch, A. et al., 2008. Causes of Interannual-Decadal Variability in the Meridional Overturning Circulation of the Midlatitude North Atlantic Ocean. *Journal of Climate,* 21(24), pp. 6599-6615.

Brüggemann, N. & Katsman, C. A., 2019. Dynamics of Downwelling in an Eddying Marginal Sea: Contrasting the Eulerian and the Isopycnal Perspective. *Journal of Physical Oceanography,* 01 November, 49(11), pp. 3017-3035.

Cunningham, S. A. et al., 2007. Temporal Variability of the Atlantic Meridional Overtuning Circulation at 26.5 N. *Science,* 17 August, 317(5840), pp. 935-938.

Gelderloos, R., Katsman, C. A. & Drijfhout, S. S., 2011. Assessing the Roles of Three Eddy Types in Restratifying the Labrador Sea after Deep Convection. *Journal of Physical Oceanography,* 01 November, 41(11), pp. 2102-2119.

Georgiou, S., 2021. *Boundary-Interior Exchanges Controlling the Labrador Sea Dynamics* , Delft, Netherlands: Delft University of Technology [PhD thesis].

Georgiou, S. et al., 2019. On the interplay between downwelling, deep convection and mesoscale eddies in the Labrador Sea. *Ocean Modelling,* 16 Februari , Volume 135, pp. 56-70.

Georgiou, S. et al., 2020. Pathways of the water masses exiting the Labrador Sea: The importance of boundary-interior exchanges. *Ocean Modelling,* 03 April.Volume 150.

Georgiou, S. et al., 2021. Direct and Indirect Pathways of Convected Water Masses and Their impacts on the Overturning Dynamics of the Labrador Sea. *Journal of Geophysical Research: Oceans,* 126(1), pp. 1-19.

Griffies, S. M. & Hallberg, R. W., 2000. Biharmonic Friction with a Smagorinsky-Like Viscosity for Use in Large-Scale Eddy-Permitting Ocean Models. *Monthly Weather Review,* 128(8), pp. 2935-2946.

Gruber, N. et al., 2019. The Oceanic Sink for Anthropogenic CO2 from 1994 to 2007. *Science,* 363(6432), pp. 1193-1199.

Katsman, C. A., Spall, M. A. & Pickart, R. S., 2004. Boundary Current Eddies and Their Role in the Restratification of the Labrador Sea. *Journal of Physical Oceanography,* 01 September, 34(9), pp. 1967-1983.

Marshall, J. et al., 1997. A finite-volume, incompressible NavierSTokes model for studies of the ocean on parallel computers. *Journal of Geophysical Research,* Volume 102, pp. 5753-5766.

Marshall, J. & Schott, F., 1999. Open-ocean convection: Observations, theory, and models.. *Reviews of Geophysics,* 37(1), pp. 1-64.

Pacini, A. et al., 2020. Mean Conditions and Seasonality of the West Greenland Boundary Current System near Cape Farewell. *Journal of Physical Oceanography,* 50(10), pp. 2849-2871.

Rykova, T., Straneo, F. & Brower, A. S., 2015. Seasonal and Interannual Variability of the West Greenland Current System in the Labrador Sea in 1993-2008. *Journal of Geophysical Research: Oceans,* Volume 120, pp. 1318-1332.

Spall, M., 2012. Influences of precipitation on water mass transformation and deep convection. *Journal of Physical Oceanography,* Volume 42, pp. 1684-1700.

Spall, M. A. & Pickart, R. S., 2001. Where Does Deep Water Sink? A Subpolar Gyre Example. *Journal of Physical Oceanography,* Volume 31, pp. 810-826.

Straneo, F., 2006. On the connection between dense water formation, overturning, and poleward heat transport in a convective basin. *Journal of Physical Oceanography,* Volume 36, pp. 1822-1840.

Talley, L. & McCartney, M., 1982. Distribution and Circulation of Labrador Sea Water. *Journal of Physical Oceanography,* 12(11), pp. 1189-1205.

The National Oceanography Centre (NOC), 2018. *Targeted Experiment to Reconcile Increased Freshwater with Increased Convection.* [Online]
Available at: https://noc.ac.uk/projects/terific
[Accessed 6 June 2021].

Van Dam, T., 2018. *Effects of a Freshening Boundary Current on Deep Convection and Eddy Activity in the Labrador Sea* , Delft: Delft University of Technology [additional thesis, masters].

Woud, S., 2020. *Effects of Salinity Variations in the Labrador Sea: An evaluation of salinity effects on the Labrador Sea circulation through an idealized model* , Delft, Netherlands: Delft University of Technology [master thesis].

Yu, L., Jin, X. & Weller, R., 2008. *Multidecade global flux datasets from the objectively analyzed air-sea fluxes (oaflux) project: latent and sensible heat fluxes, ocean evaporation, and related surface meteorological variables,* Woods Hole: Woods Hole Oceanographic Institute.

Zhang, R., 2010. Latitudinal dependence of Atlantic meridional overturning circulation (AMOC) variations. *Geophysical Research Letters,* 37(16).

APPENDICES

APPENDIX A

A.1. Derivation of inflow conditions

Geostrophic balance for zonal velocity:

$$\boldsymbol{u} = -\frac{1}{f\rho_0}\frac{\partial p}{\partial y} \qquad [A.1]$$

Hydrostatic balance:

$$\frac{\partial p}{\partial z} = -\rho g \qquad [A.2]$$

Take derivative of Eq. [A.1] with respect to z:

$$\frac{\partial \boldsymbol{u}}{\partial z} = -\frac{1}{f\rho_0}\frac{\partial^2 p}{\partial y \partial z} \qquad [A.3]$$

Substitution of Eq. [A.2] in Eq. [A.3] gives the thermal wind balance:

$$\frac{\partial \boldsymbol{u}}{\partial z} = \frac{g}{f\rho_0}\frac{\partial \rho}{\partial y} \qquad [A.4]$$

Next the linear equation of state (for temperature only) is defined as:

$$\rho = \rho_0\big(1 - \alpha(\mathrm{T} - \mathrm{T}_0)\big) = \rho_0(1 - \alpha\Delta\mathrm{T}) \qquad [A.5]$$

And the derivative of the equation of state with respect to y is:

$$\frac{\partial \rho}{\partial y} = \frac{\partial \rho_0\big(1 - \alpha(\mathrm{T} - \mathrm{T}_0)\big)}{\partial y} = \frac{\partial(\rho_0 - \alpha\rho_0\mathrm{T} + \alpha\rho_0\mathrm{T}_0)}{\partial y} = -\alpha\rho_0\frac{\partial \mathrm{T}}{\partial y} \qquad [A.6]$$

Filling in the derivative of Eq. [A.6] into the thermal wind balance of Eq. [A.4] yields the shear velocity expressed in terms of the temperature gradient along the y-direction (instead of density gradient):

$$\frac{\partial \boldsymbol{u}}{\partial z} = -\frac{\alpha g}{f}\frac{\partial \mathrm{T}}{\partial y} \qquad [A.7]$$

The initial temperature profile in y- and z-direction is prescribed with a hyperbolic tangent relationship in y-direction and a linear relationship in z-direction similar to Katsman et al. (2004):

$$\mathrm{T}_{ini}(y,z) = \mathrm{T}_{ref}(z) - \frac{\Delta\rho}{2\alpha\rho_0}\left(1 - \frac{z}{z_b}\right)\left[1 + \tanh\left(\frac{y - y_0}{\mathrm{L}_y}\right)\right]$$

[A.8]

Where the factor $\Delta\rho/\alpha\rho_0$ comes from rewriting the linear equation of state Eq. [A.5]:

$$\rho = \rho_0(1 - \alpha\Delta\mathrm{T}) = \rho_0 - \alpha\rho_0\Delta\mathrm{T}$$

$$\Delta\mathrm{T} = -\frac{(\rho - \rho_0)}{\alpha\rho_0} = -\frac{\Delta\rho}{\alpha\rho_0}$$

[A.9]

The factor $1/2$ comes from the choice of the temperature profile in y-direction in Katsman et al. (2004). Taking the derivative with respect to y-direction of Eq. [A.8]:

$$\frac{\partial \mathrm{T}}{\partial y} = -\frac{\Delta\rho}{2\alpha\rho_0 \mathrm{L}_y}\left(1 - \frac{z}{z_b}\right)\frac{1}{\cosh^2\left(\frac{y - y_0}{\mathrm{L}_y}\right)}$$

[A.10]

Substitution of the expression for $\partial\mathrm{T}/\partial y$ in Eq. [A.7] gives:

$$\frac{\partial \boldsymbol{u}}{\partial z} = \frac{g\Delta\rho}{2f\rho_0 \mathrm{L}_y}\left(1 - \frac{z}{z_b}\right)\frac{1}{\cosh^2\left(\frac{y - y_0}{\mathrm{L}_y}\right)}$$

[A.11]

Integration over z gives the initial zonal velocity profile:

$$\boldsymbol{u}(y,z) = \int\left[\frac{g\Delta\rho}{2f\rho_0 \mathrm{L}_y}\left(1 - \frac{z}{z_b}\right)\frac{1}{\cosh^2\left(\frac{y - y_0}{\mathrm{L}_y}\right)}\right]\mathrm{d}z$$

$$\boldsymbol{u}(y,z) = \frac{g\Delta\rho}{2f\rho_0 \mathrm{L}_y}\frac{1}{\cosh^2\left(\frac{y - y_0}{\mathrm{L}_y}\right)}\int\left(1 - \frac{z}{z_b}\right)\mathrm{d}z$$

$$\boldsymbol{u}(y,z) = \frac{g\Delta\rho}{2f\rho_0 \mathrm{L}_y}\frac{1}{\cosh^2\left(\frac{y - y_0}{\mathrm{L}_y}\right)}\left(z - \frac{z^2}{2z_b} + \mathrm{C}\right)$$

[A.12]

With C the integration constant. Prescribing that $u(y, z_b) = 0$ leaves:

$$\boldsymbol{u}(y,z_b) = \frac{g\Delta\rho}{2f\rho_0 \mathrm{L}_y}\frac{1}{\cosh^2\left(\frac{y - y_0}{\mathrm{L}_y}\right)}\left(z_b - \frac{z_b^2}{2z_b} + \mathrm{C}\right) = 0 \rightarrow \mathrm{C} = -\frac{z_b}{2}$$

Rewriting Eq. [A.12] now yields the initial zonal velocity profile:

$$\mathbf{U}_{ini}(y,z) = \frac{g\Delta\rho}{2f\rho_0 \mathrm{L}_y}\frac{1}{\cosh^2\left(\frac{y - y_0}{\mathrm{L}_y}\right)}\left(z - \frac{z^2}{2z_b} - \frac{z_b}{2}\right)$$

Taking out the factor 2 between brackets and multiplying numerator and denominator with z_b:

$$\mathbf{U}_{ini}(y,z) = \frac{g\Delta\rho}{4f\rho_0 \mathrm{L}_y} \frac{1}{\cosh^2\left(\frac{y-y_0}{\mathrm{L}_y}\right)} \frac{\left(2zz_b - \frac{z^2 z_b}{z_b} - z_b^2\right)}{z_b}$$

$$\mathbf{U}_{ini}(y,z) = -\frac{g\Delta\rho}{4f\rho_0 \mathrm{L}_y} \frac{1}{\cosh^2\left(\frac{y-y_0}{\mathrm{L}_y}\right)} \frac{(z-z_b)^2}{z_b}$$

[A.13]

APPENDIX B

B.1. Along-isopycnal integration of passive tracer originating from the interior

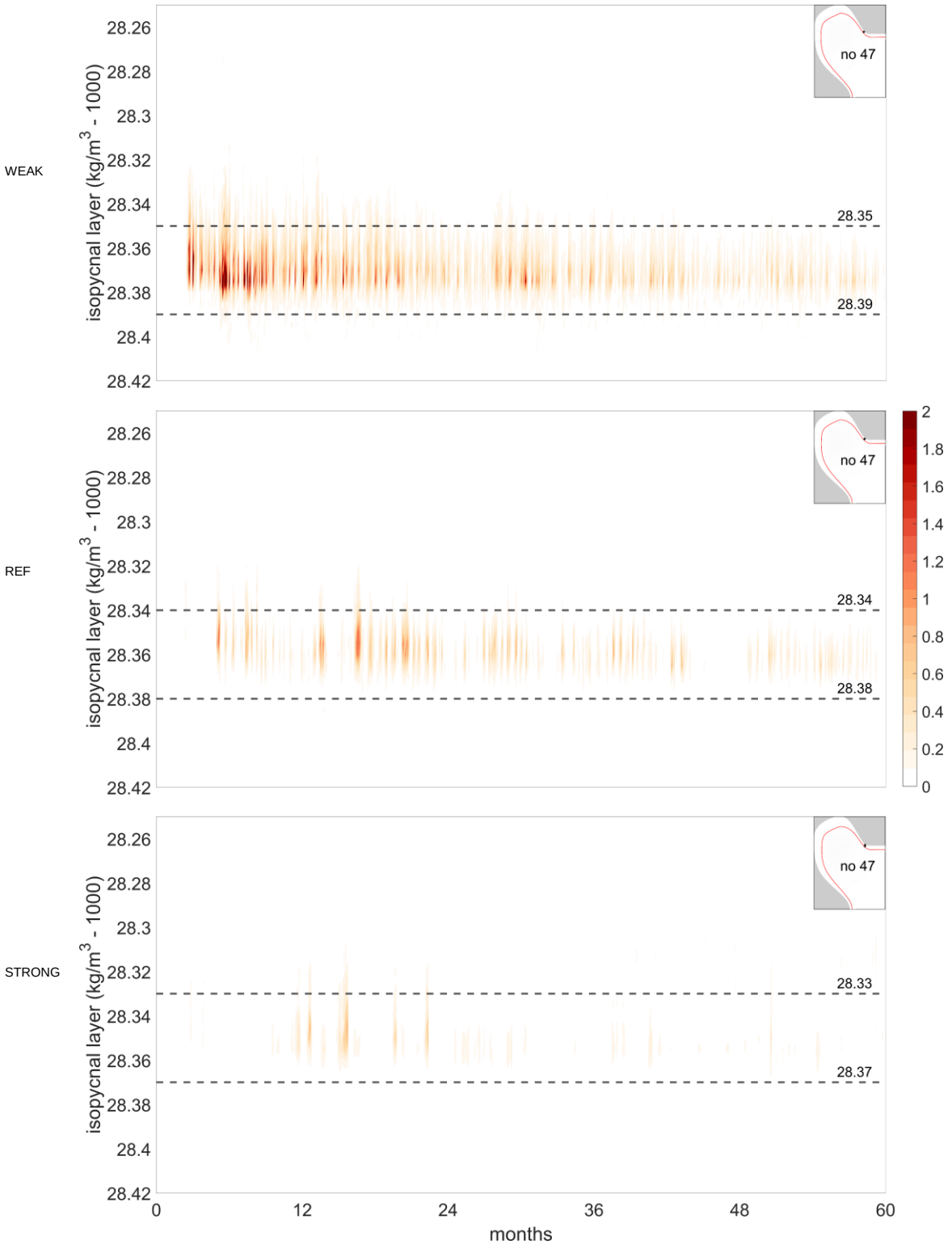

Figure B.1 Amount of passive tracer transported by the boundary current within different isopycnal layers over five years after release. The signal is a combination of tracer 1 + 2. The boundary current is defined by the barotropic streamfunction for contour line 17 Sv (WEAK), 18 Sv (REF), 19 Sv (STRONG). The location of the section is highlighted on the inset. Black dashed lines denote limits of convective waters per scenario.

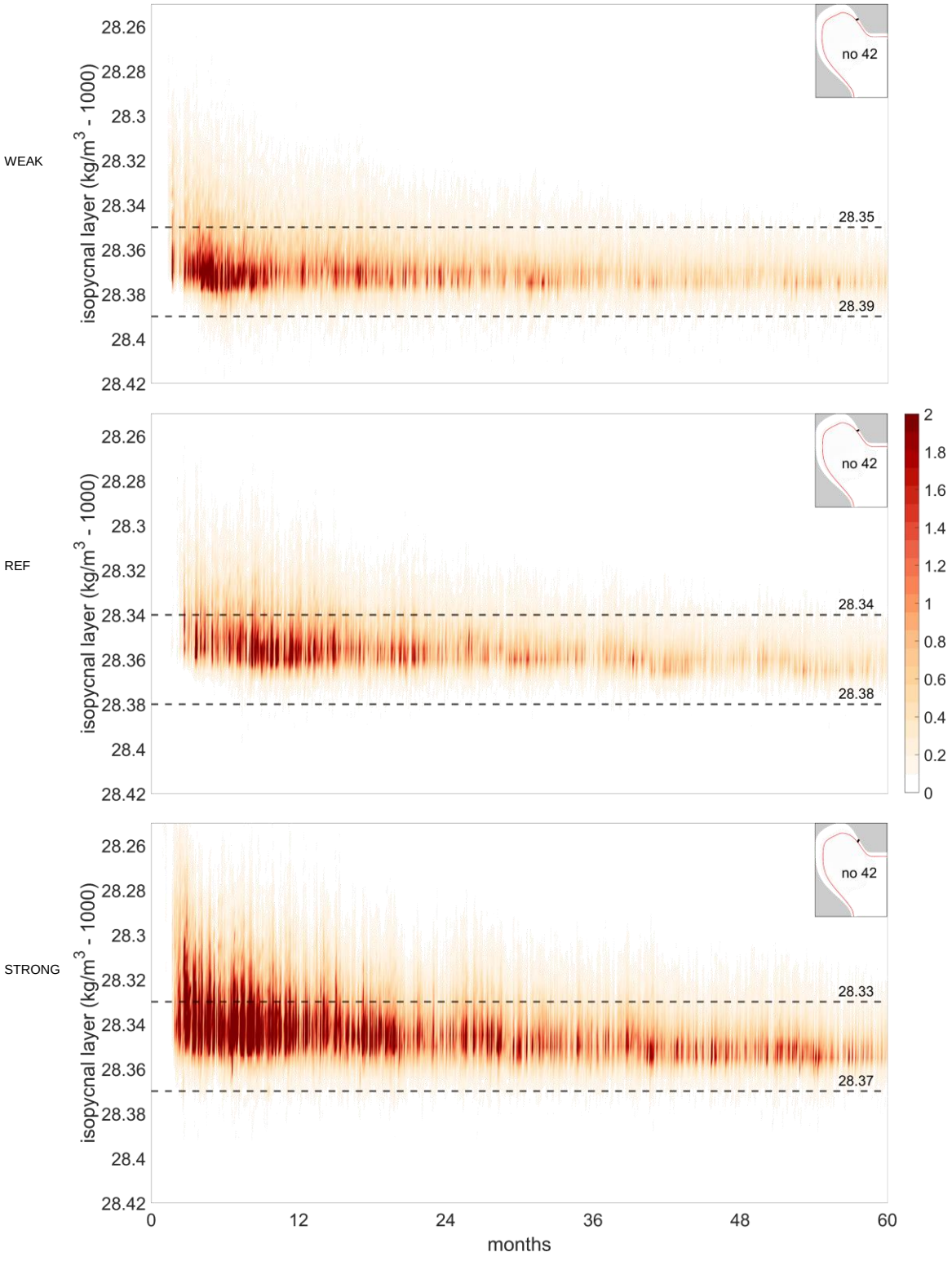

Figure B.2 Same as Figure B.1, but for a different cross-section (more downstream).

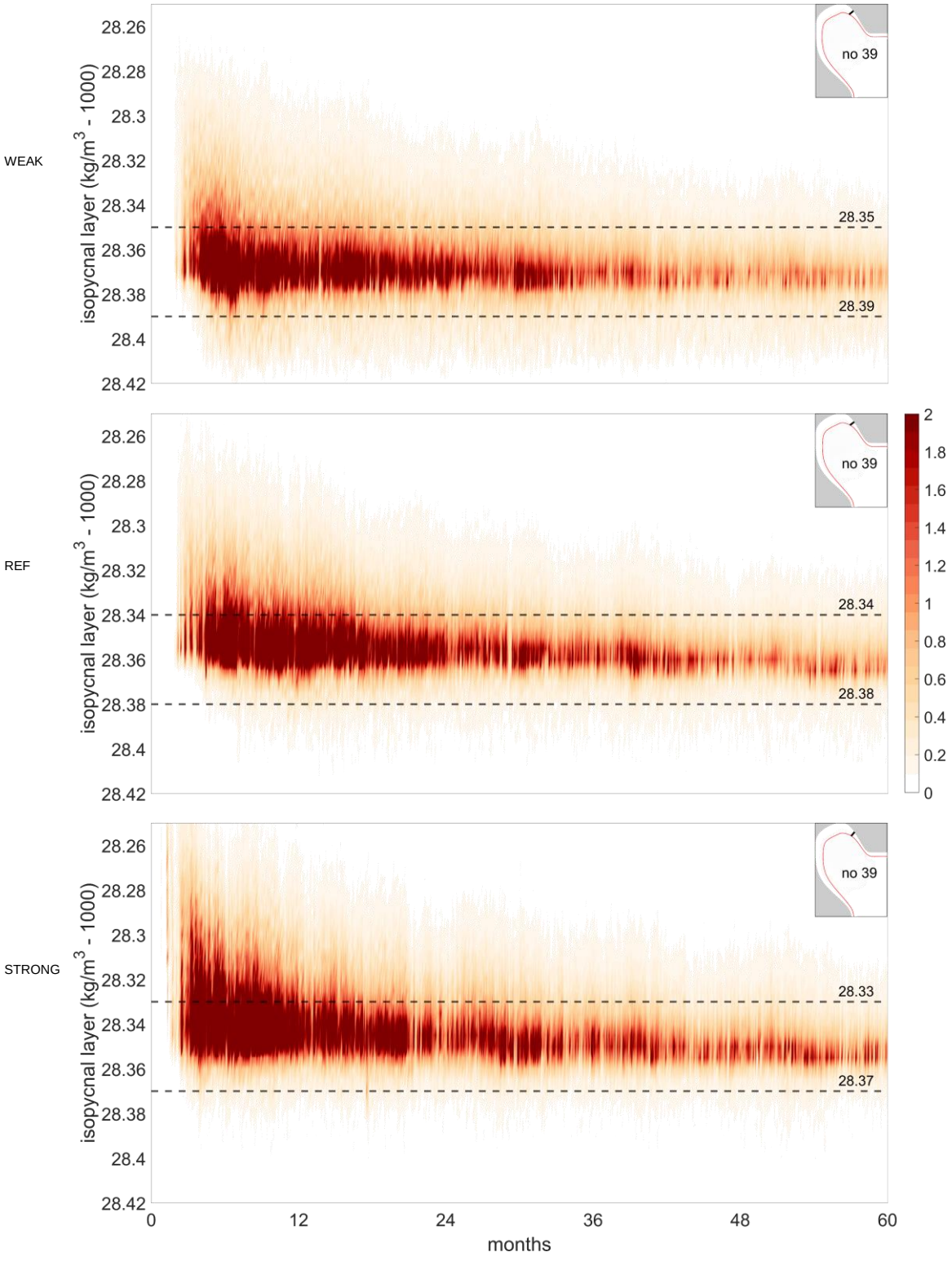

Figure B.3 Same as Figure B.1, but for a different cross-section (more downstream).

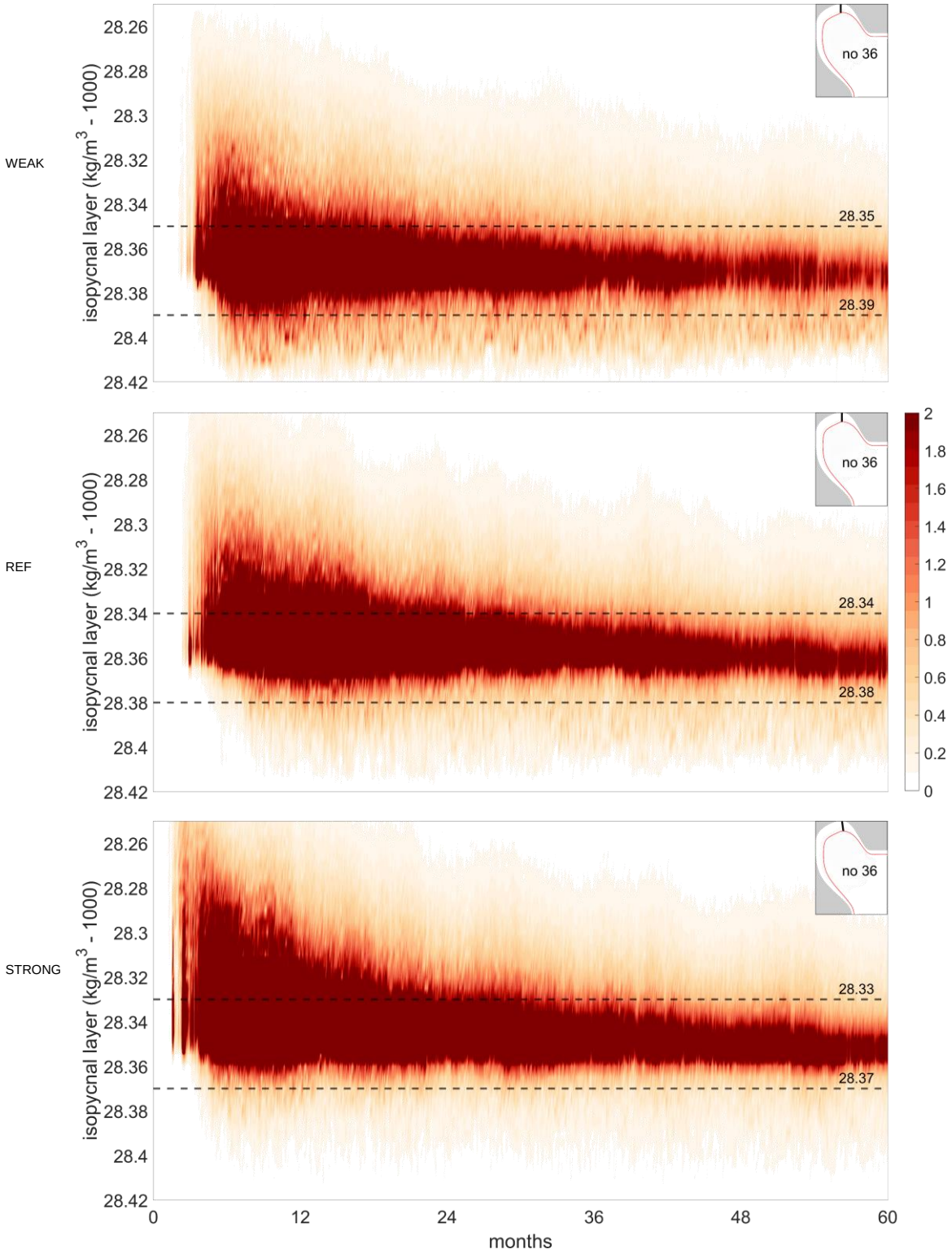

Figure B.4 Same as Figure B.1, but for a different cross-section (more downstream).

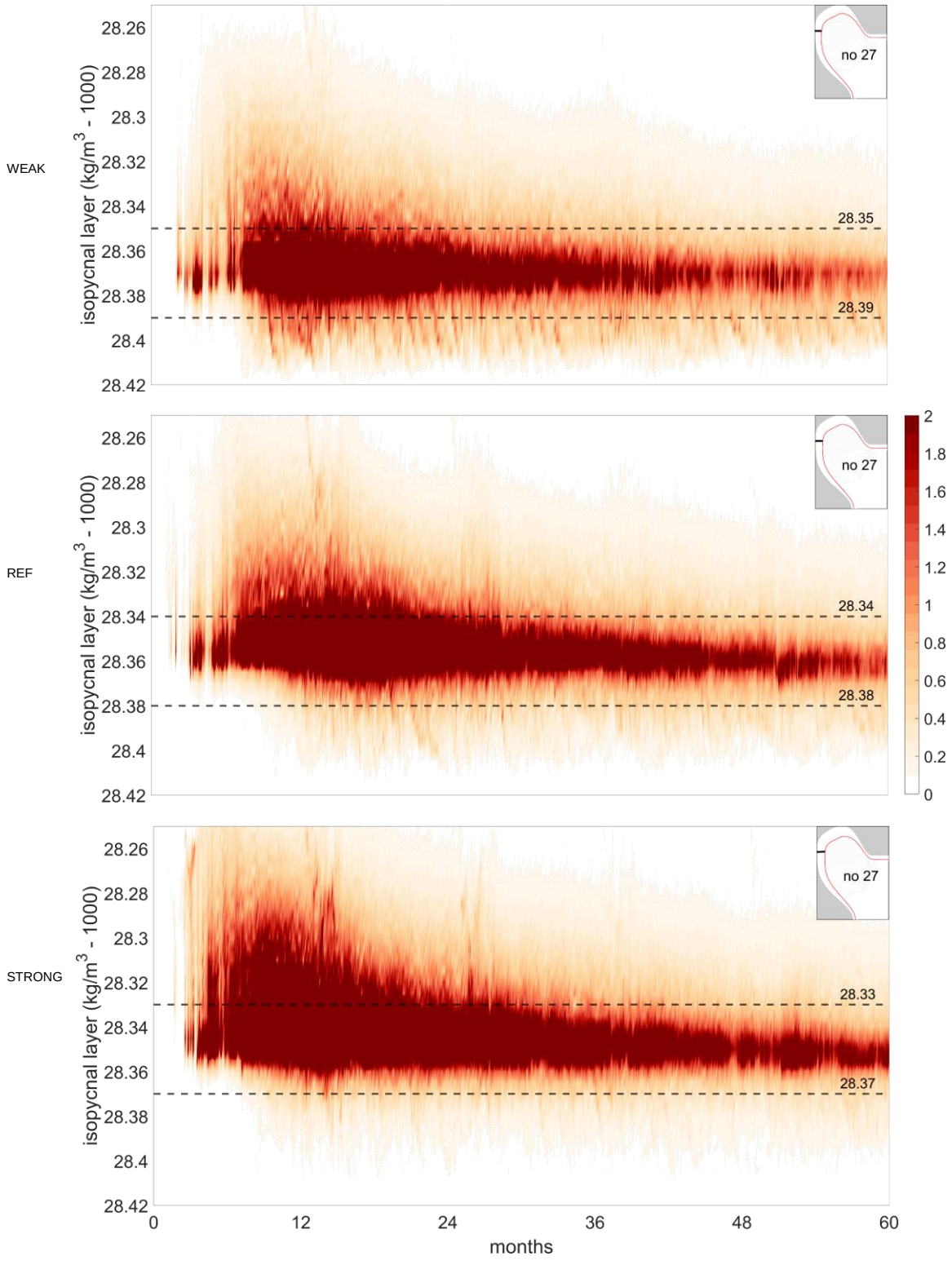

Figure B.5 Same as Figure B.1, but for a different cross-section (more downstream).

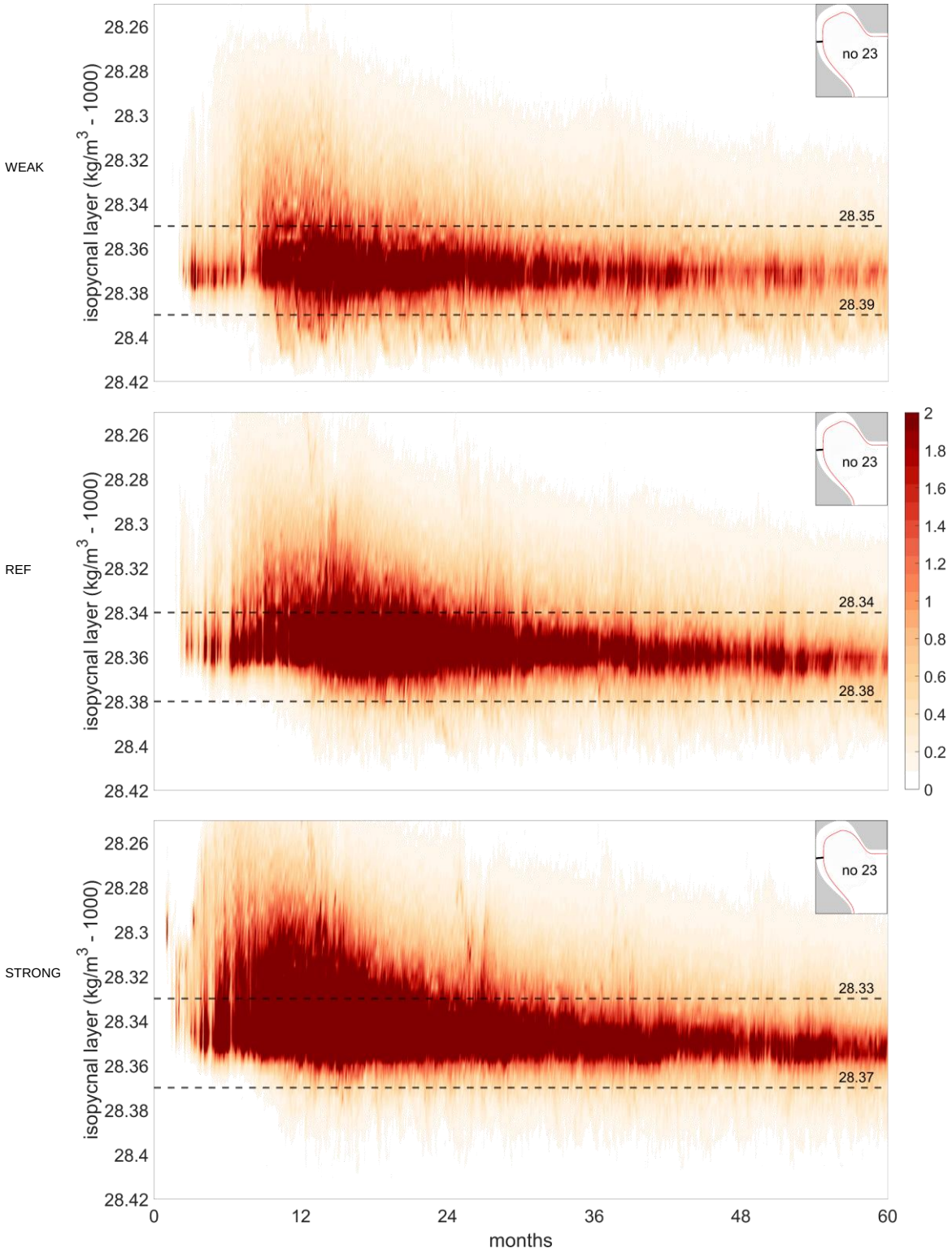

Figure B.6 Same as Figure B.1, but for a different cross-section (more downstream).

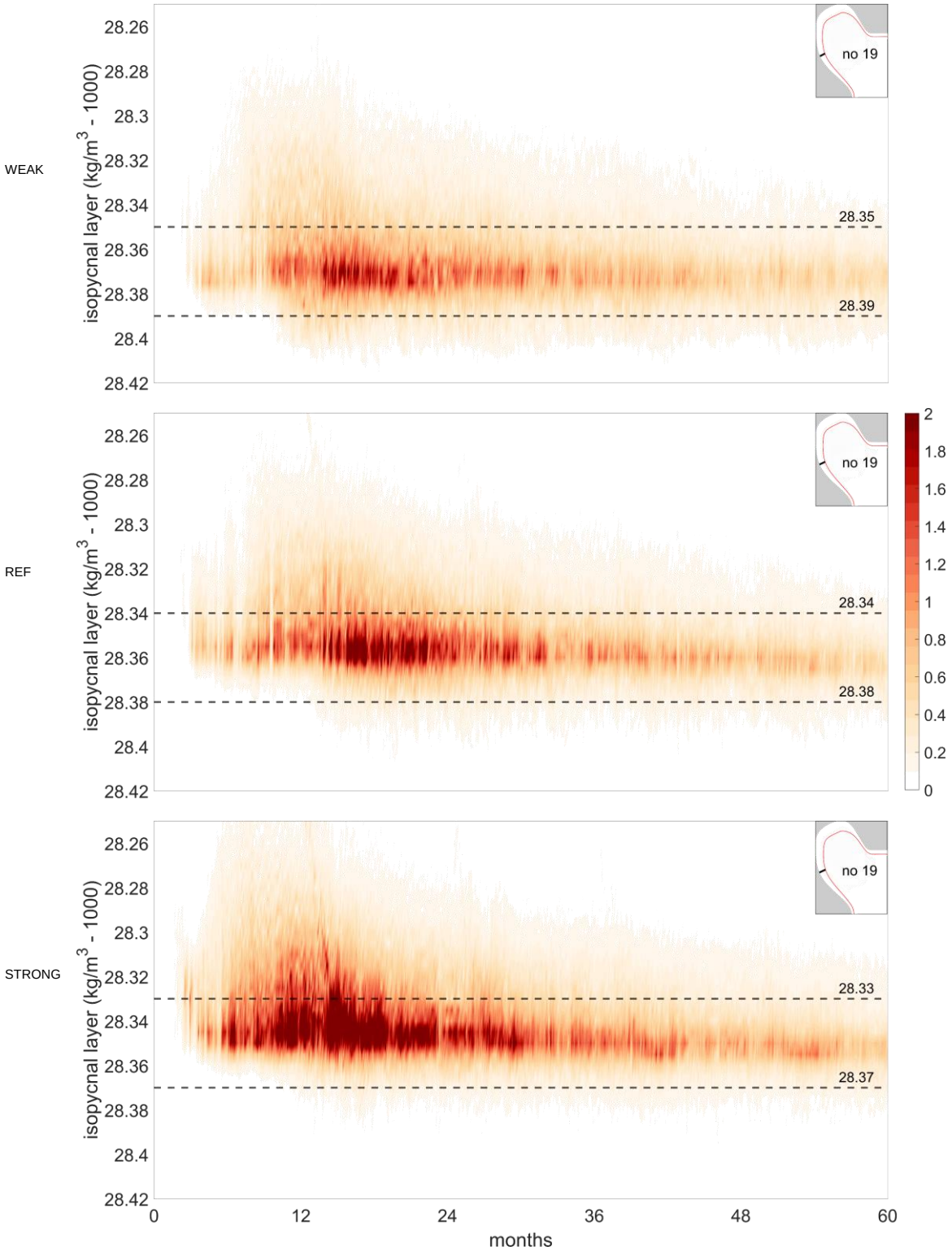

Figure B.7 Same as Figure B.1, but for a different cross-section (more downstream).